A Parametric Study of Hypersonic Waverider Flight Mechanics in Optimized Trajectories during Atmospheric Entry

UNDERGRADUATE HONORS RESEARCH THESIS

Presented in Partial Fulfillment of the Requirements for the Degree Bachelor of Science with Honors Research Distinction in the College of Engineering of The Ohio State University

By

Jonathan H. Richmond

Aeronautical and Astronautical Engineering

The Ohio State University

2021

Thesis Defense Committee:

Dr. Clifford A. Whitfield, Advisor

Dr. Datta Gaitonde

Abstract

Over the years, many aerospace corporations and agencies have attempted to develop hypersonic vehicles. However, until recently, they have only achieved very limited success due to a lack of air-breathing hypersonic propulsion technology. Now, as technology is advancing and funds are becoming more available, aviation is once again shifting its focus towards hypersonic flight. One of many hypersonic applications is atmospheric reentry, whether reentry into Earth's atmosphere or entry into another planetary body's atmosphere. While basic theories on hypersonic reentry flight mechanics are already in use, these analyses have yet to be applied to optimizing trajectories for hypersonic waveriders in skip-glide atmospheric entry trajectories. The purpose of this research project was to provide a brief analysis of unpowered skip and glide entry trajectories and to present an optimized hypersonic waverider trajectory for a simple atmospheric reentry scenario. Five main types of unpowered glide trajectories—constant flight path angle, constant sinking speed, constant flight speed, constant dynamic pressure, and constant heating rate—were analyzed using MATLAB to model the altitude, velocity, flight path angle, and lift modulation profiles. Additionally, constant aerodynamic efficiency skip trajectories were analyzed for their ability to extend reentry ranges. The results of these analyses were then used to optimize a combined skip-glide atmospheric reentry trajectory for hypersonic waveriders about the Earth's equator. This research utilized a classical optimization approach, using MATLAB to graph the applicable design spaces for the analysis. The resulting trajectory maximizes the range of the reentry trajectory while conforming to applied maximum aerodynamic heating and maximum dynamic pressure constraints. The findings of this research will benefit the aerospace community by providing insight into hypersonic waverider performance during Earth reentry after completed space

missions. This information can be used to inform flight vehicle design decisions for optimizing hypersonic waverider performance. Moreover, beyond just Earth atmospheric reentry, the analyses used in this research can also be applied to atmospheric entry into other planetary atmospheres, aiding in vehicle design and planning for interplanetary missions.

Dedication

To my supportive family, girlfriend, and advisors that made this research thesis possible.

Acknowledgments

First, I would like to thank my research professor and mentor, Dr. Clifford Whitfield, for the incredible opportunity to conduct undergraduate research with him and his research group. This experience has allowed me to discover more about myself and my interests within the field of aerospace engineering and to explore past the limits of the classroom. I am grateful for the time and energy he put into developing my research project with me and guiding me as we stepped into uncharted territory. I would also like to thank my other committee member, Dr. Datta Gaitonde, for his time and input on the final stages of my thesis.

I would also like to thank The Ohio State University's Eminence Fellows program and the College of Engineering for the opportunity to attend the university and for the funding to conduct my own undergraduate research. I would like to give a special thanks to my program coordinator, Rebecca Ward, for helping and encouraging me throughout my college journey, especially as I began looking for research opportunities. Her invaluable time and advice helped get me to where I am today.

I would like to extend special gratitude to my mom and dad for their support throughout my entire life. I know I would not have made it to this university and accomplished what I have without their tireless guidance and support. I would also like to acknowledge and thank my good friend and colleague Isaac, who has provided feedback and support throughout this research process as well as my undergraduate studies. Finally, I would like to thank my amazing girlfriend Grace, whose advice and encouragement have helped me push forward through everything. I am very grateful for everything these people have done for me.

Table of Contents

List of Tables

List of Figures

Nomenclature

Symbols

g	Acceleration of gravity
h	Altitude
m	Mass
q	Time rate of heat input per unit area
$\bar{q}$	Nondimensional time rate of heat input per unit area
r	Distance from center of planetary body
s	Unified theory nondimensional range parameter
t	Time
u	Unified theory nondimensional altitude parameter
$\bar{u}$	Chapman's nondimensional altitude parameter
v	Unified theory nondimensional velocity parameter
w	Unified theory nondimensional altitude parameter
x	Range
A	Surface area
C_D	Drag coefficient
C_F	Skin friction coefficient
C_L	Lift coefficient
E	Aerodynamic efficiency (lift-to-drag ratio)
M	Mean molecular weight
P	Pressure

P_d	Dynamic pressure
Q	Heat transferred
R	Radius of curvature
$\mathscr{R}$	Universal gas constant
S	Reference surface area
T	Temperature
V	Flight speed
Z	Unified theory nondimensional density parameter
$\bar{Z}$	Chapman's nondimensional density parameter
β	Reciprocal of scale height
γ	Flight path angle
γ_I	Modified flight path angle
η	Unified theory nondimensional density parameter
θ	Range angle
κ	Constant for stagnation temperature heat transfer
λ	Rescaled lift coefficient
ρ	Atmospheric density
σ	Bank angle
φ	Latitude
ψ	Heading angle
ω	Longitude

Scripts

X^*	Value corresponding to maximum lift-to-drag ratio
X_0	Sea level value
X_{av}	Average value
X_f	Final value
X_i	Initial value
X_r	Ratio
X_s	Stagnation value

Abbreviations

ARV	Ascent and reentry vehicle
ASTV	Aeroassisted space transfer vehicle
CV	Cruise vehicle
FVDT	Flight Vehicle Design and Testing
NASA	National Aeronautics and Space Administration
RV	Reentry vehicle

Chapter 1: Introduction

1.1 Introduction

Hypersonic flight is the aerospace industry's next big frontier. Over the past several decades, the world has witnessed speed and efficiency improvements in subsonic flight, an increase in supersonic aircraft and technologies, and even extraordinary feats of space travel and exploration. While continued improvements and new technology development in all three of these areas remain vital to the success of both commercial and federal aerospace sectors, it is also critical to invest in the largely unexplored domain of hypersonic flight.

Although little experimental data and research on hypersonic flight exists, it is not a new field of study. The study of hypersonic flight first began in 1946 when the term "hypersonic" was coined in a paper by Tsien. However, it was not until the early 1960s that hypersonic flight vehicles first became discussed as a means for orbital reentry vehicles. These were proposed as an alternative to the low aerodynamic efficiency capsules, such as Mercury and Gemini, which had little range and control. The U.S. Air Force started the Dyna-Soar program in 1957 to research manned, high-speed gliders with high aerodynamic efficiencies to provide more maneuverability, range, and control. Unfortunately, the program ran into technical problems and delays, and was terminated in 1963. However, one good outcome of the program was the Space Shuttle. Developed in the 1970s and 80s, it was able to decrease the cost of space flight by increasing range capabilities and control [1].

In response to the technical challenges facing high-speed gliders, the National Aeronautics and Space Administration (NASA) attempted to develop sustained powered hypersonic flight instead. To accomplish this, the administration started researching supersonic combustion ramjet

(scramjet) technology as an air-breathing propulsion method for hypersonic flight. In the end, the program cost $50 million with nominal results. Bertin and Cummings call it “a graphic example of what happens when an immature technology is pushed too fast too soon” [1]. Without air-breathing propulsion for sustained flight, any hypersonic testing of vehicle configurations from that point relied on rocket propulsion, which remained expensive and inflexible.

Until recently, reliable hypersonic propulsion systems did not exist. Even now they are still in the developing stages and not commercially available. The only available option in the past was rocket technology, which was expensive and difficult to control, limiting its usefulness in hypersonic testing [2]. Now that the necessary technologies are in development, it is pivotal to devote time and resources to reestablish research into hypersonic flight mechanics and design studies of hypersonic flight vehicle airframes.

According to a paper by Bertin and Cummings, there are three main mission goals centered on defense capabilities for hypersonic atmospheric flight and efficient access to space:

1. Deliver decisive blows at the outset of hostilities, with the goal of destroying the adversary’s ability to fight a protracted war.
2. Deliver cost-effective weapons to defeat time-critical targets and to establish in-theater dominance, if a protracted war cannot be avoided.
3. Maintain flexible, readily accomplished access to space [1].

While the three above goals focus on military benefits, they also translate to the public and private sectors. The main advantages of controlled hypersonic flight include new opportunities that come with increased speeds, improved flight efficiency, and atmospheric reentry maneuverability. In addition, Bertin and Cummings propose that hypersonic flight research should aim to increase nine

attributes of flight: affordability, availability, capability, certifiability, environmental compatibility, maintainability, operability, predictability, and reliability [1]. By keeping these attributes in mind during research and design, any progress made in the field of hypersonic flight will also inevitably advance other aerospace domains.

So, what is different this time around? To begin with, now that so much progress has been made in other aerospace domains, the U.S. is willing to allocate more funds and resources towards the research of hypersonic flight and vehicle design. Many commercial companies also now have the resources and motivation to conduct independent research and development on the subject. In addition, the technologies that were missing in the past are now in development and will soon be readily available for utilization. Finally, as other nations are once again investing in hypersonic flight research, it is important for the U.S. to remain at the forefront of aerospace research and development in order to maintain its defense capabilities and advance technology for everyone across the globe.

In particular, reestablishing research in the field of hypersonic atmospheric reentry flight mechanics would be beneficial. As interest in space exploration resurges, with new endeavors to send humans to Mars and other planetary bodies, there is a growing need for maneuverable atmospheric entry vehicles. Like the Space Shuttle, these vehicles would enable their pilots to effectively glide over a long range, and control how they approach a surface and where they land, adding much needed flexibility and efficiency to human missions. Additionally, considering the advancements of competing nations in the areas of sustained atmospheric hypersonic flight, this research would also aid in the design and control of maneuverable hypersonic missiles to be used in the Earth’s atmosphere.

1.2 Background

1.2.1 Hypersonic Flight

The term “hypersonic” is commonly applied to vehicles, projectiles, or air flow (in the case of a wind tunnel) having speeds greater than five times the speed of sound (Mach 5). Like supersonic flows, hypersonic flows create shock waves when they interact with objects in the flow stream. However, a major difference is that at such high speeds, the thermodynamic energy of the individual particles inside the flow is much greater than the overall kinetic energy of the flow [1]. Due to the high flow temperatures resulting from the larger thermodynamic energy in hypersonic flow, air molecules tend to dissociate into their individual atoms and can ionize. Large Mach numbers, extreme temperatures, and dissociation of molecules, which can occur before and after Mach 5, characterize the hypersonic flow regime and separate it from subsonic and supersonic flows, resulting in a need for different analytical methods [3].

The various challenges and applications provided by hypersonic flight have led to four main classes of hypersonic flight vehicles: winged reentry (RV), cruise (CV), ascent and reentry (ARV), and aeroassisted space transfer vehicles (ASTV) [1]. Figure 1.1 on the following page shows the altitude and velocity ranges that these vehicle types operate in, as well as which aerothermodynamic effects dominate the flow in each region. In addition to various flight vehicles, there are a few propulsion systems that could potentially operate in hypersonic conditions such as air-breathing scramjets, rockets, electric engines, or hybrid systems. As part of this research, the technology readiness levels of these propulsion systems will be examined later.

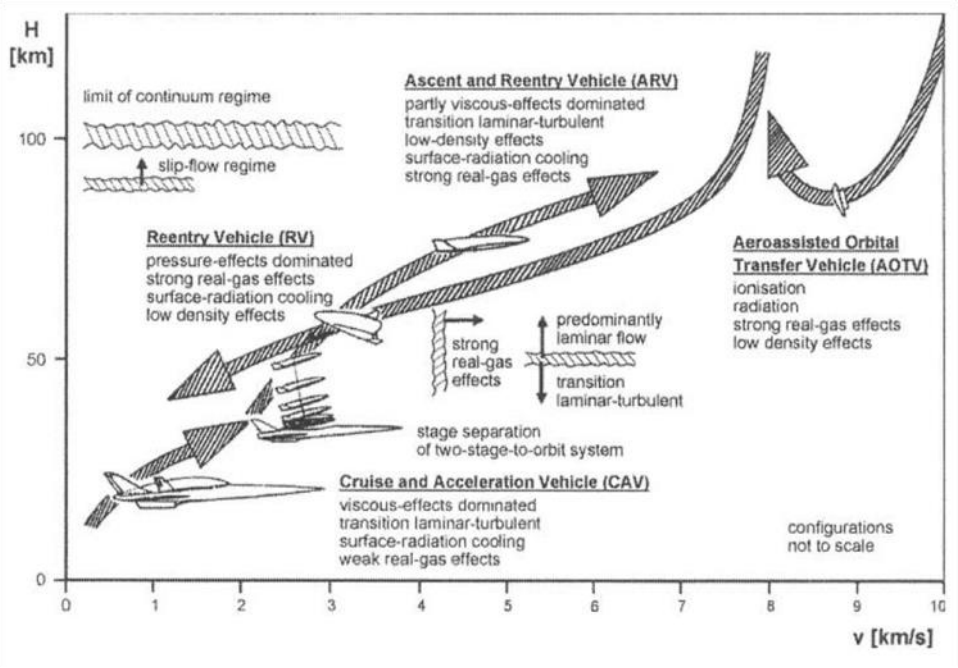

Figure 1.1: Four major classes of hypersonic vehicles and aerothermodynamic characteristics [4]

1.2.2 Waveriders

Since this research will focus mainly on the flight mechanics of atmospheric entry, the most relevant hypersonic flight vehicles are winged RVs. One such RV is a high aerodynamic efficiency waverider, which will be the main example in this research. The main purpose of a waverider is to trap the shock wave attached to the leading edge of the vehicle under its body. The pressure increase caused by the shock wave generates additional lift, increasing the overall aerodynamic efficiency of the vehicle. In addition, since shock waves have very little physical interaction with the body of the vehicle, this process does not introduce significantly more heating [2]. Essentially, this hypersonic flight vehicle "rides" its own shock wave, which is how it gets its name. Figure 1.2 below illustrates the difference between a waverider body and generic hypersonic vehicle.

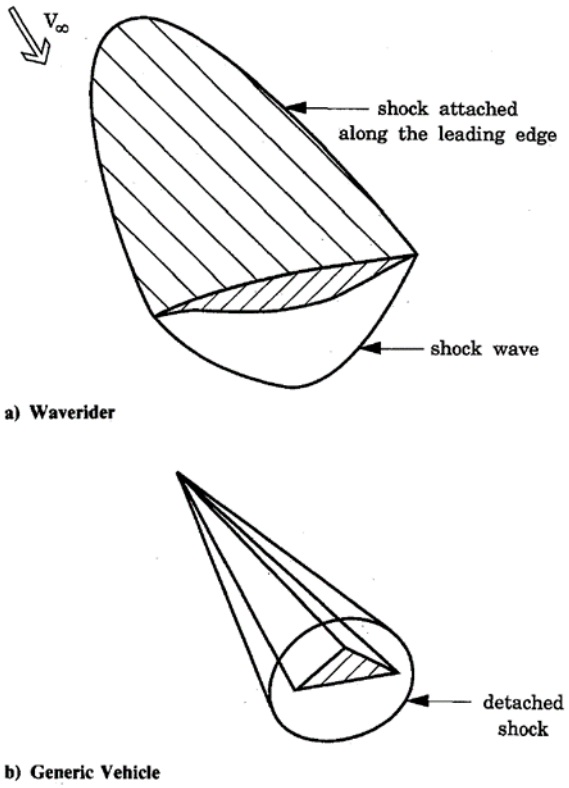

Figure 1.2: Comparison of waverider and generic hypersonic vehicle [5]

After first developing the concept in 1951, Nonweiler determined in 1962 that the waverider's wings needed to angle down at the tips. This would form a single flat plate shock under the aircraft to provide the lift. In 1978, while adding to Nonweiler's research, Kuchemann realized that at a speed of Mach 8, a waverider could travel nonstop to the farthest point on Earth [2]. Since then, several potential applications of waveriders for planetary exploration have been researched. This past research includes analyses of waveriders and their use in planetary atmospheres [5,6,7], long-range hypervelocity performance [8], long-range periodic cruise trajectories [9,10], and planetary skip-glide trajectories [2]. Additionally, previous work also

includes trajectory optimizations for reentry glide [11], boost-glide [12], and morphable waveriders [13], as well as onboard trajectory planning [14]. Building upon these previous analyses, this research will use hypersonic atmospheric reentry flight mechanics to maximize the trajectory range for waveriders in unpowered atmospheric reentry.

Because the shape of a waverider is designed to trap its shock wave under the fuselage, waverider designs are optimized to provide target aerodynamic efficiencies for specific flight parameters, which include Mach number, angle of attack, viscosity, and atmospheric density. Figure 1.3 below and Figure 1.4 on the following page are just two examples of hypersonic waverider designs. The shape of the fuselage and the wings change depending on the optimization parameters and methods chosen [2].

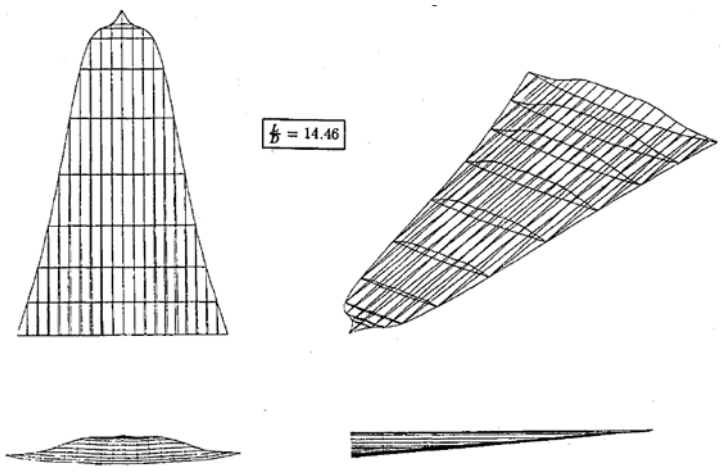

Figure 1.3: Waverider designed for the atmosphere of Venus [5]

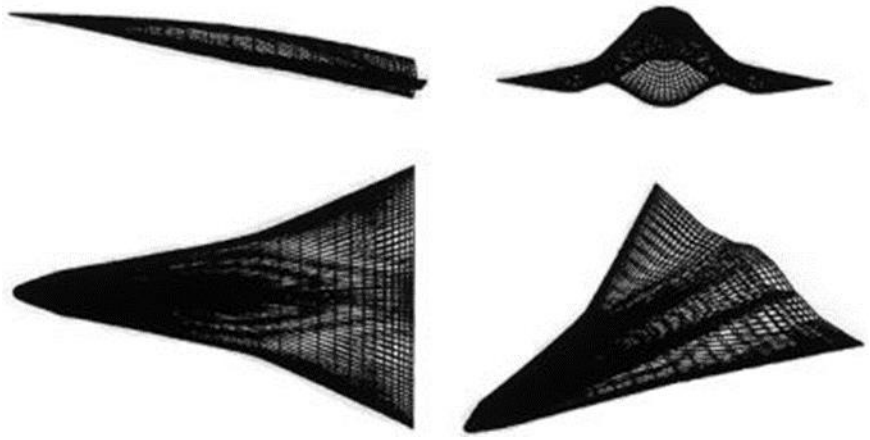

Figure 1.4: Waverider designed using osculating cones method [6]

1.2.3 Trajectories

In the scope of this research, three main unpowered trajectory types will be examined during atmospheric entry: ballistic, glide, and skip. The first of these, the ballistic trajectory, forms a parabola extending past the atmosphere over a planetary body, with a powered ascent and unpowered descent segment. With this type of trajectory, negligible lift is generated due to the high reentry angle. During a glide trajectory, the hypersonic flight vehicle uses the lift it generates to glide down to the surface, lengthening its range. In a skip trajectory, the vehicle "skips" off the surface of the atmosphere, using its unique trajectory to avoid heat buildup from the atmosphere and extend the overall flight range. Theoretically, a hypersonic waverider could skip as many times as needed to fulfill mission requirements. Figure 1.5 on the next page shows an example of a skip-glide trajectory, which is a string of ballistic and skip trajectories that ends in a glide. Since waveriders are lift-generating vehicles, this research will focus mainly on glide and skip-glide trajectories [2].

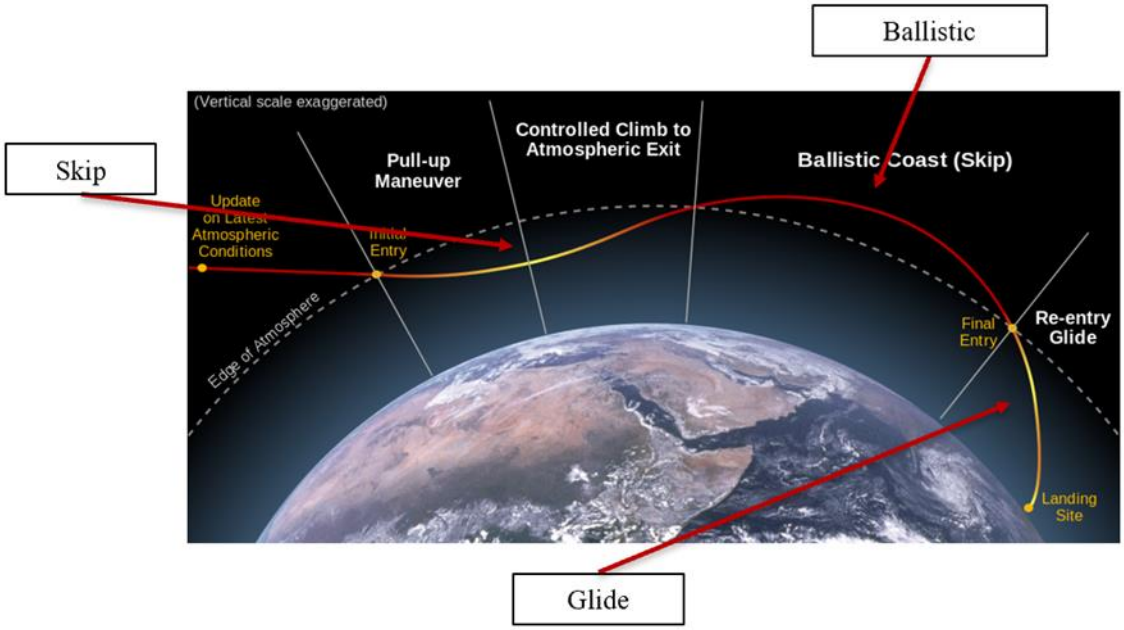

Figure 1.5: Atmospheric entry trajectory types [15]

1.3 Research Motivation and Goals

Up until now, hypersonic flight research has focused on which trajectory types would lead to the greatest range in foreign atmospheres. However, more foundational parametric research is still needed for applying hypersonic reentry flight mechanics to optimizing trajectory range when considering all other criteria. This research will focus on flight mechanics and trajectories encompassing hypersonic atmospheric reentry in support of the Flight Vehicle Design and Testing (FVDT) Group at The Ohio State University. The development of parametric results determined from the flight mechanics will provide efficiency when optimizing flight trajectories and hypersonic waverider designs.

There are three primary objectives of this research: (1) analyze the flight mechanics, aerodynamic heating, and dynamic pressure of hypersonic vehicles during atmospheric entry, (2)

compare parametric trade studies for various glide trajectory types, and (3) optimize skip-glide entry trajectories for specified parameters within the determined design space for a given scenario. To accomplish these three goals, this research was divided into three main phases. First, hypersonic atmospheric entry flight mechanics were analyzed based on previous literature. Using these models, a performance analysis was conducted to create parametric trade studies of parameters relevant to hypersonic reentry. This analysis was used along with established constraints to calculate optimized reentry trajectories using a classical "graphical" optimization approach [16,17].

Chapter 2: Flight Mechanics Analysis

2.1 Atmospheric Model

The first main engineering assumption made in this research was modeling planetary atmospheres as purely exponential with regard to pressure and density. Since atmospheric density and pressure play important roles in the analysis of hypersonic flight mechanics, treating their relationship with the altitude as exponentially decreasing greatly simplifies the analysis. Approximating these properties in this way, maximum relative error can still be kept below about 25%, which is sufficient for most preliminary vehicle design [18].

Atmospheric temperature, pressure, and density are related through Equation 2.1 and Equation 2.2 below.

$$P = \rho \frac{\mathcal{R}}{M} T \quad (2.1)$$

$$dP = -\rho g dr \quad (2.2)$$

Manipulating these two equations and factoring in the above engineering assumption, Equation 2.3 below can be derived.

$$\frac{\rho}{\rho_0} = e^{-\beta(r-r_0)} \quad (2.3)$$

If β is assumed to be constant, this equation clearly shows how atmospheric density decreases exponentially. This constant, which is the reciprocal of the scale height, is a characteristic of each planetary atmosphere. For instance, the mean scale height for the Earth's atmosphere is 7100m, while it is about 25000m for Jupiter. The atmospheric pressure follows a similar relationship to the density [19].

Often, an isothermal atmosphere is also assumed to further simplify the analysis [18,19]. With an isothermal atmosphere, the speed of sound and dynamic viscosity, two other properties important to flight mechanics, also remain approximately constant.

2.2 Hypersonic Flight Mechanics Theory

2.2.1 Chapman's Theory

This research mainly utilized equations based on Chapman's theory, as explained by Vinh, Busemann, and Culp, to analyze hypersonic atmospheric reentry flight mechanics [19]. As a linear, second-order differential equation, Chapman's equation provides enough accuracy for initial vehicle design while only requiring simple assumptions. It accomplishes this by nondimensionalizing key variables, removing the need to account for a specific flight vehicle's physical characteristics.

Chapman begins his derivation with the two kinematic equilibrium equations of motion shown in Equation 2.4 and Equation 2.5 below.

$$\frac{dV}{dr} = -\frac{\rho S C_D V}{2m \sin\gamma} - \frac{g}{V} \quad (2.4)$$

$$\frac{d\gamma}{dr} = \frac{\rho S C_L}{2m \sin\gamma} + \left(1 - \frac{gr}{V^2}\right)\frac{\cos\gamma}{r \sin\gamma} \quad (2.5)$$

These equations describe motion in a vertical plane using coordinates tangential to the flight path. Using these equations, the change in velocity, V, and change in flight path angle, γ, are related to the change in the radial distance from the center of the planetary body in question.

To simplify these equations, Chapman makes a few basic assumptions. The first is that a fractional change in radial distance is much smaller than the fractional change in horizontal velocity. This assumption is valid if the aerodynamic forces create a rapid change in speed

regardless of the flight path angle. If the flight vehicle in question is a lifting vehicle, then Chapman also assumes that the horizontal lift component is much smaller than the corresponding drag component, which is valid for the three trajectory types utilized in this research. Finally, Chapman's equation utilizes the basic assumption of an inverse square gravitational force field and an exponential atmosphere [19].

As mentioned earlier, Chapman's equation uses nondimensionalized variables to simplify calculations. The nondimensionalization of these variables are shown below in Equation 2.6 and Equation 2.7. In his equation, $\bar{Z}$ becomes the dependent variable while $\bar{u}$ is the independent variable.

$$\bar{Z} = \frac{\rho S C_D}{2m}\sqrt{\frac{r}{\beta}}\bar{u} \quad (2.6)$$

$$\bar{u} = \frac{V\cos\gamma}{\sqrt{gr}} \quad (2.7)$$

With these variables, the equilibrium equations of motion simplify to Chapman's first equation, Equation 2.8 below, which is used to evaluate the flight path angle.

$$\frac{d\bar{Z}}{d\bar{u}} - \frac{\bar{Z}}{\bar{u}} = \sqrt{\beta r}\sin\gamma \quad (2.8)$$

This equation can be rewritten as Chapman's second-order nonlinear differential equation, shown below in Equation 2.9.

$$\bar{u}\frac{d^2\bar{Z}}{d\bar{u}^2} - \left(\frac{d\bar{Z}}{d\bar{u}} - \frac{\bar{Z}}{\bar{u}}\right) - \frac{\left(1-\bar{u}^2\right)(\cos\gamma)^4}{\bar{Z}\bar{u}} + \sqrt{\beta r}\frac{C_L}{C_D}(\cos\gamma)^3 + \frac{\bar{u}(\cos\gamma)^2(\sin\gamma)^2\gamma}{\bar{Z}} +$$

$$\sqrt{\beta r}\frac{C_L}{C_D}\cos\gamma\,(\sin\gamma)^2 = 0 \quad (2.9)$$

Chapman's second equation, shown below in Equation 2.10, is a combination of Equations 2.8 and Equation 2.9, taking the earlier stated assumptions into account. The result is another nonlinear differential equation.

$$\bar{u}\frac{d^2\bar{Z}}{d\bar{u}^2} - \left(\frac{d\bar{Z}}{d\bar{u}} - \frac{\bar{Z}}{\bar{u}}\right) = \frac{\left(1-\bar{u}^2\right)}{\bar{Z}\bar{u}}(\cos\gamma)^4 - \sqrt{\beta r}\frac{C_L}{C_D}(\cos\gamma)^3 \qquad (2.10)$$

On the left-hand side of the equation, the first term represents the vertical acceleration of the flight vehicle, while the term counteracting it is the vertical drag component. On the other side, the third term characterizes the gravitational force minus the centrifugal force and the final term is the lift force. Although this equation is applicable for nonlifting vehicles with any flight path angles, for lifting vehicles, it is only applicable under Chapman's assumptions.

To use either of these equations, the solutions must be integrated numerically. Only the initial flight path angle and value of $\bar{u}$ are needed since the initial value of $\bar{Z}$ is 0. The numerical results for various entry conditions can be tabulated and used for any arbitrary flight vehicle in the Earth's atmosphere [20]. These results can also be extrapolated for other atmospheres if the flight path angle is small. Using these values, several useful quantities can be calculated, such as acceleration, altitude, dynamic pressure, Reynolds number, aerodynamic heating, and time of flight [19].

2.2.2 Unified Theory for Entry into Planetary Atmospheres

Vinh, Busemann, and Culp also discuss the unified theory for entry into planetary atmospheres [19]. This theory describes the performance of lifting flight vehicles without needing specific physical characteristics of the flight vehicle. Using equations with universal variables, this theory applies to three-dimensional entry trajectories into arbitrary atmospheres without relying

on the assumptions made by Chapman [20]. Because all three dimensions are now being described, instead of just planar motion, momentum equilibrium equations of motion are required in addition to the kinematic ones.

For the purposes of this theory, the planetary body and its atmosphere are assumed to be nonrotating spheres. The gravitational field is still assumed to be an inverse square and the atmospheric density is still assumed to decrease exponentially. However, this theory does not require Chapman's other main assumptions, allowing it to be applied to more scenarios. Another difference between the two theories is the nondimensionalized constants. This unified theory uses three nondimensionalized variables, shown in Equations 2.11-13 below, two of which are variations of Chapman's variables while one is a new independent variable, *s*.

$$Z = \frac{\rho S C_D}{2m}\sqrt{\frac{r}{\beta}} \quad (2.11)$$

$$u = \frac{V^2(\cos\gamma)^2}{gr} \quad (2.12)$$

$$s = \int_0^t \frac{V}{r}\cos\gamma\, dt \quad (2.13)$$

For atmospheric entry under constant lift and drag, this new independent variable is always increasing.

Using the aforementioned basic assumptions, the equilibrium equations of motion can be rewritten in relation to the three nondimensionalized variables, shown in Equations 2.14-19 below and on the next page.

$$\frac{dZ}{ds} = -\beta r Z \tan\gamma \quad (2.14)$$

$$\frac{du}{ds} = -\frac{2\sqrt{\beta r}Zu}{\cos\gamma}\left[1 + \frac{C_L}{C_D}\cos\sigma\tan\gamma + \frac{\sin\gamma}{2\sqrt{\beta r Z}}\right] \quad (2.15)$$

$$\frac{d\gamma}{ds} = \frac{\sqrt{\beta r}Z}{\cos\gamma}\left[\frac{C_L}{C_D}\cos\sigma + \frac{\cos\gamma}{\sqrt{\beta r}Z}\left(1 - \frac{(\cos\gamma)^2}{u}\right)\right] \quad (2.16)$$

$$\frac{d\omega}{ds} = \frac{\cos\psi}{\cos\varphi} \quad (2.17)$$

$$\frac{d\varphi}{ds} = \sin\psi \quad (2.18)$$

$$\frac{d\psi}{ds} = \frac{\sqrt{\beta r}Z}{(\cos\gamma)^2}\left[\frac{C_L}{C_D}\sin\sigma - \frac{(\cos\gamma)^2\cos\psi\tan\varphi}{\sqrt{\beta r}Z}\right] \quad (2.19)$$

These six equilibrium equations of motion are restricted to constant lift-to-drag ratios and are considered exact equations for atmospheric entry [19]. Like with Chapman's theory, numerical solutions for *Z* have been computed and tabulated using initial *u*, flight path angle, and lift-to-drag ratio [21].

2.2.3 Flight with Lift Modulation

The two theories presented above share the major assumption of constant lift-to-drag ratio, caused by constant angle of attack and constant bank angle. If the flight vehicle is allowed to control its lift profile during atmospheric entry via changes in angle of attack and bank angle, then the unified theory for entry into planetary atmospheres can be expanded and used to study a variety of flight scenarios.

Vinh, Busemann, and Culp introduce this theory of flight with lift and bank angle modulation by redefining Chapman's two nondimensionalized parameters [19]. The new definitions are shown in Equation 2.20 below and Equation 2.21 on the following page, where the asterisk denotes correspondence to maximum lift-to-drag ratio.

$$Z = \frac{\rho S C_L^*}{2m}\sqrt{\frac{r}{\beta}} \quad (2.20)$$

$$v = \frac{u}{(\cos\gamma)^2} = \frac{V^2}{gr} \quad (2.21)$$

In this analysis, *s* is still the independent variable. With these new nondimensionalized variables, the new equations of equilibrium are shown in Equations 2.22-27 below, where *f(λ)* denotes the appropriate drag polar function.

$$\frac{dZ}{ds} = -\beta r Z \tan\gamma \quad (2.22)$$

$$\frac{dv}{ds} = -\frac{2\sqrt{\beta r}Zvf(\lambda)}{E^* \cos\gamma} - (2 - v)\tan\gamma \quad (2.23)$$

$$\frac{d\gamma}{ds} = \frac{\sqrt{\beta r}Z}{\cos\gamma}\left[\frac{C_L}{C_L^*}\cos\sigma + \frac{\cos\gamma}{\sqrt{\beta r}Z}\left(1 - \frac{1}{v}\right)\right] \quad (2.24)$$

$$\frac{d\omega}{ds} = \frac{\cos\psi}{\cos\varphi} \quad (2.25)$$

$$\frac{d\varphi}{ds} = \sin\psi \quad (2.26)$$

$$\frac{d\psi}{ds} = \frac{\sqrt{\beta r}Z\frac{C_L}{C_L^*}\sin\sigma}{(\cos\gamma)^2} - \cos\psi\tan\varphi \quad (2.27)$$

With the use of lift and bank angle modulation, entry trajectories can be controlled to achieve desired requirements such as constant glide angle, constant rate of descent, or constant heating rate [19]. The characteristics of each of these scenarios will be explored later.

2.2.4 Lateral Maneuverability

During atmospheric entry, lifting flight vehicles can change their heading and move in a lateral direction by rotating the lifting force out of the vertical plane. Changing the lateral heading of the flight path affects the maximum range of the flight vehicle, so this research is particularly interested in the maximum coverable surface area on the planetary body. The main theory behind

lateral maneuverability used is derived from the theory of flight with lift and bank angle modulation presented by Vinh, Busemann, and Culp [19].

A condition of equilibrium glide is desirable to achieve maximum range for an unpowered, lifting flight vehicle. Under these conditions, the flight path angle is small and nearly constant, which simplifies the equilibrium equations of motion presented earlier in Equations 2.22-27. These four new equilibrium equations, shown in Equations 2.28-31 below, are the basis for determining maximum lateral range.

$$\frac{dv}{ds} = -\frac{(1-v)\left[1+\left(\frac{C_L}{C_L^*}\right)^2\right]}{E^*\frac{C_L}{C_L^*}\cos\sigma} \quad (2.28)$$

$$\frac{d\omega}{ds} = \frac{\cos\psi}{\cos\varphi} \quad (2.29)$$

$$\frac{d\varphi}{ds} = \sin\psi \quad (2.30)$$

$$\frac{d\psi}{ds} = \frac{1-v}{v}\tan\sigma - \cos\psi\tan\varphi \quad (2.31)$$

From the above equations, it can be inferred that to minimize the decrease in speed, v, the flight vehicle should operate at maximum lift-to-drag ratio during its glide. In addition, to achieve maximum lateral range, the bank angle, σ, should be modulated in an optimal manner. To simplify calculations, it is assumed that an average constant bank angle can be used to provide a comparable performance. It is also assumed that the changes in heading, ψ, and latitude, φ, are small. With these simplifications, the equation for speed can be integrated to produce Equation 2.32 below.

$$v = 1 - (1 - v_0)e^{\left(\frac{2s}{E^*\cos\sigma}\right)} \quad (2.32)$$

Using the speed as the new independent variable, a linear second-order differential equation can be derived to calculate the lateral range, shown in Equation 2.33 on the next page.

$$\frac{d^2\varphi}{dv^2} - \frac{1}{1-v}\frac{d\varphi}{dv} + \frac{E^{*^2}(\cos\sigma)^2}{4(1-v)^2}\varphi = \frac{E^{*^2}\sin\sigma\cos\sigma}{4v(1-v)} \quad (2.33)$$

Once integrated, this equation produces the final solution for final range, Equation 2.34, which can be further simplified for small maximum lift-to-drag ratios, Equation 2.35 below.

$$\frac{48\varphi}{E^{*^2}\pi^2} = \sin(2\sigma)\left[1 - \frac{3E^{*^2}(\cos\sigma)^2}{2\pi^2}\sum_{n=1}^{\infty}\frac{1}{n^2\left[n^2+\frac{E^{*^2}}{4}(\cos\sigma)^2\right]}\right] \quad (2.34)$$

$$\varphi = \frac{E^{*^2}\pi^2}{48}\sin(2\sigma) \quad (2.35)$$

From Equation 2.35, it can also be seen that the optimal average bank angle is 45° [19].

With regards to the maximum footprint of the flight vehicle, the maximum area reachable is a zone between positive and negative maximum lateral range. If the lateral range is small, then the equilibrium conditions are simplified to Equations 2.36-38 below, where the control law in Equation 2.39 is used for integration.

$$\frac{d\omega}{dv} = -\frac{E^*\cos\sigma\cos\psi}{2(1-v)} \quad (2.36)$$

$$\frac{d\varphi}{dv} = -\frac{E^*\cos\sigma\sin\psi}{2(1-v)} \quad (2.37)$$

$$\frac{d\psi}{dv} = -\frac{E^*\sin\sigma}{2v} \quad (2.38)$$

$$\tan\sigma = \frac{1-v}{v}\frac{\tan(\theta_f-\theta)}{\sin\psi} \quad (2.39)$$

2.3 Aerodynamic Heating

All flight vehicles have a maximum total heat they can absorb before structural damage or damage to the payload occurs. In addition, the maximum rate of aerodynamic heating and the maximum dynamic pressure are also important quantities to consider as they affect structural

performance. Besides velocity and altitude, aerodynamic heating also heavily depends on the specific flight vehicles shape and material. Vinh, Busemann, and Culp use Allen and Eggers' analysis of aerodynamic heating, in which they focus on three main aspects: total heat input, time rate of average heat input per unit area, and time rate of local stagnation region heat input per unit area [19, 22].

Allen and Eggers make several assumptions to simplify their analysis. The first is that although aerodynamic heat transfer is composed of convective and radiative heating, the radiation factor is negligible. In addition, real gas effects and shock-wave boundary layer interactions are ignored, an assumption applicable up until about 3 kilometers per second. Under these same conditions, it can also be assumed that the Reynolds analogy applies and that the Prandtl number is unity. While these assumptions will not lead to exact aerodynamic heating results, they will produce an estimate adequate for preliminary design [22].

Once again, nondimensionalized variables are used to develop first-order solutions for aerodynamic heating. Equation 2.40 and Equation 2.41 below introduce those variables.

$$u = \frac{1}{2}\left(\frac{V^2}{g_i r_i}\right) \quad (2.40)$$

$$\eta = \frac{SC_D}{2m\beta}\rho \quad (2.41)$$

Using these nondimensionalized variables, the equations for the three main aerodynamic heating parameters are as shown in Equations 2.42-44 below and on the next page.

$$Q = \frac{AC_F}{2}\left(\frac{m}{SC_D}\right) g_i r_i (u_i - u) \quad (2.42)$$

$$q_{av} = \frac{\sqrt{2}m\beta}{SC_D}(g_i r_i)^{\frac{3}{2}} C_F \eta u^{\frac{3}{2}} \quad (2.43)$$

$$q_s = \frac{4\kappa}{\sqrt{R}}\sqrt{\frac{m\beta}{SC_D\rho_0}}\eta^{\frac{1}{2}}u^{\frac{3}{2}} \quad (2.44)$$

Depending on the trajectory constraints, these equations can also be simplified further, and used for comparison between different trajectories [19,22].

Chapter 3: Glide Reentry Trajectory Studies

3.1 Reentry Trajectories

As stated earlier, there are three main types of reentry trajectories shown below in Figure 3.1. Ballistic missiles travel a nonlifting, parabolic trajectory with high flight path angles while skip trajectories are just series of glide trajectories connected by powered boosts to skip in and out of the atmosphere. Since this research explores hypersonic flight vehicles with lifting bodies, it will focus on five main constraining glide trajectories as well as combined skip-glide trajectories.

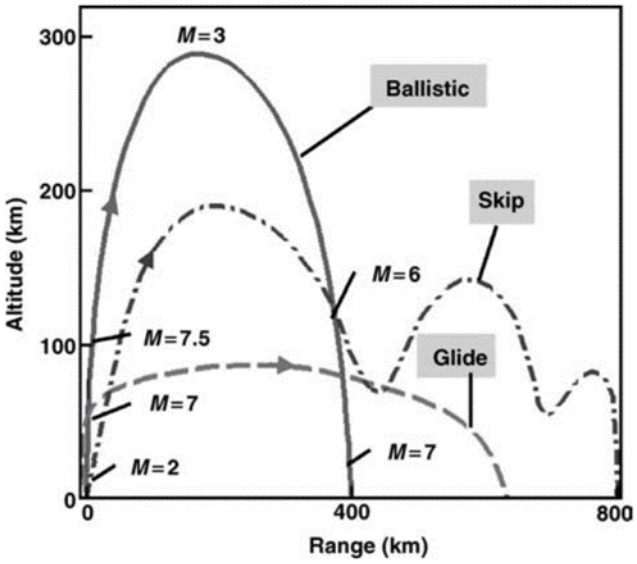

Figure 3.1: Trajectory Types and Example Altitudes [3]

3.2 Constrained Trajectory Cases

3.2.1 Constant Flight Path Angle

The first glide trajectory case of interest is one where the flight path angle is held constant. Figure 3.2, Figure 3.3, and Figure 3.4 on the following pages, created in MATLAB, compare the altitude, velocity, and lift modulation profiles vs. surface distance for a few constant flight path angle trajectories in Earth's atmosphere. Note that these are represented by nondimensionalized variables, including two new ones defined in Equation 2.45 and Equation 2.46 below.

$$w = \frac{2m}{\rho S C_L^* r} \quad (2.45)$$

$$\lambda = \frac{C_L}{C_L^*} \quad (2.46)$$

In addition, the altitude profile figure shows an approximate limit for the Earth's atmosphere at about 100km above the surface. Due to the nondimensionalization of the scenario, the trends seen in these figures can also be applied to other atmospheres.

As seen in these figures, increasing the magnitude of the constant flight path angle decreases the flight range (as expected). The velocity profile is dramatically affected by these changes: a lower constant flight path angle will allow the flight vehicle to naturally decelerate more as it descends. Low flight path angles also require a more gradual change in the lift provided. Based on these figures alone, it seems that a low constant flight path angle produces the best results in terms of range and natural deceleration for constant flight path angle trajectories.

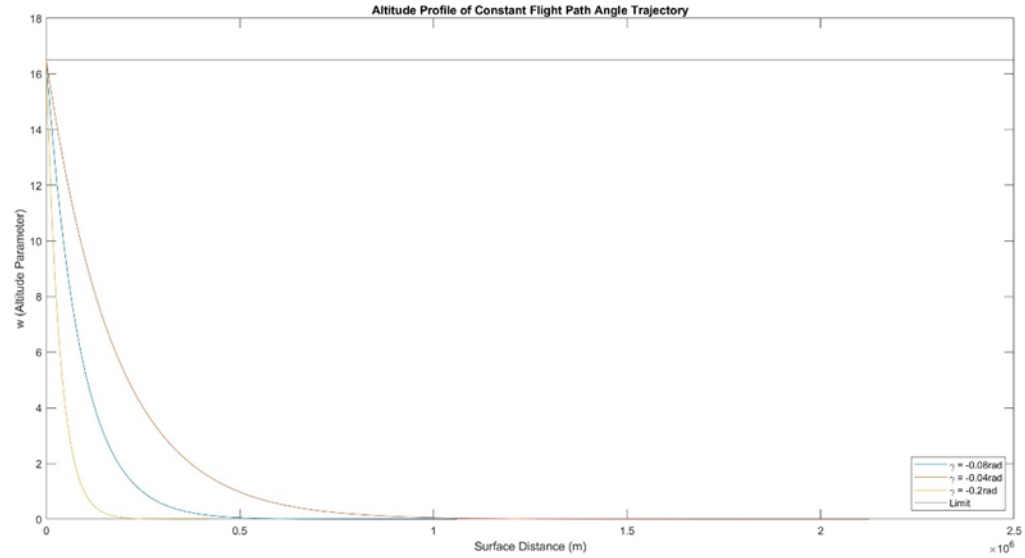

Figure 3.2: Altitude Profile of Constant Flight Path Angle Trajectories

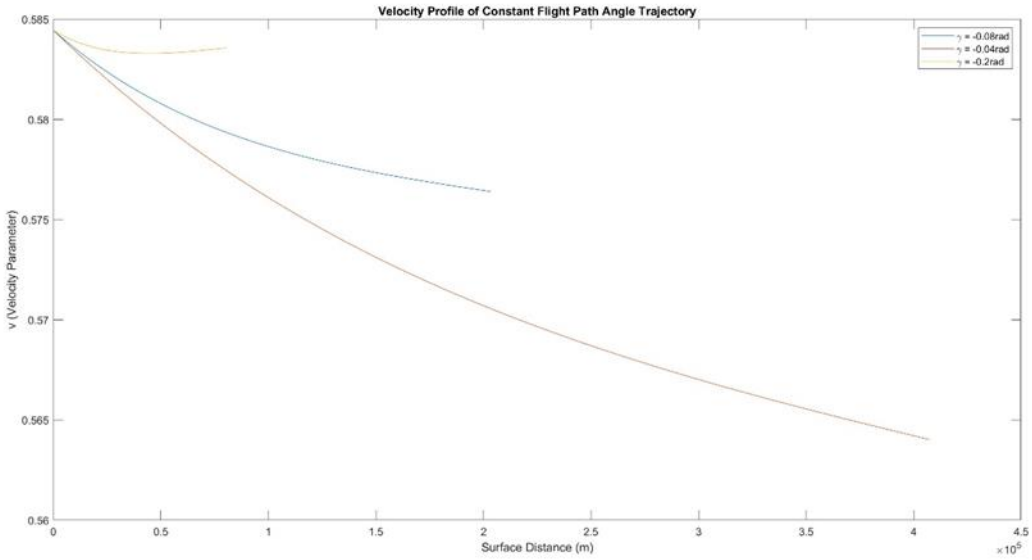

Figure 3.3: Velocity Profile of Constant Flight Path Angle Trajectories

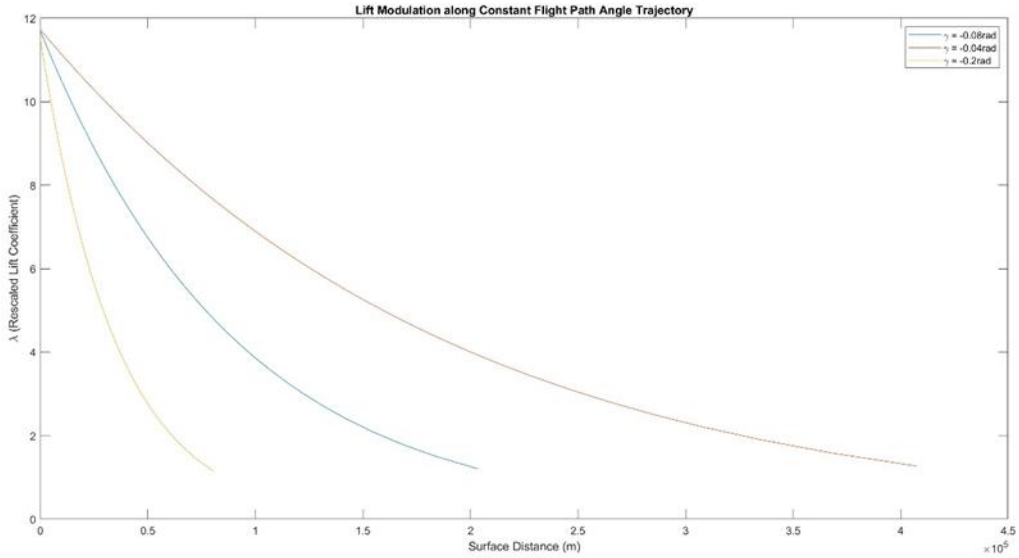

Figure 3.4: Lift Modulation along Constant Flight Path Angle Trajectories

3.2.2 Constant Sinking Speed

Constant sinking speed (or constant rate of descent) trajectories hold to a constant vertical velocity described in Equation 2.47 below where C represents some constant.

$$v(\sin\gamma)^2 = C \quad (2.47)$$

Figure 3.5, Figure 3.6, Figure 3.7, and Figure 3.8 on the following pages show the altitude, velocity, flight path angle, and lift modulation profiles for constant sinking speed. Since this type of trajectory is used much closer to the planet's surface to control the flight vehicle's approach velocity, the plotted trajectories begin at about 10km above the Earth's surface.

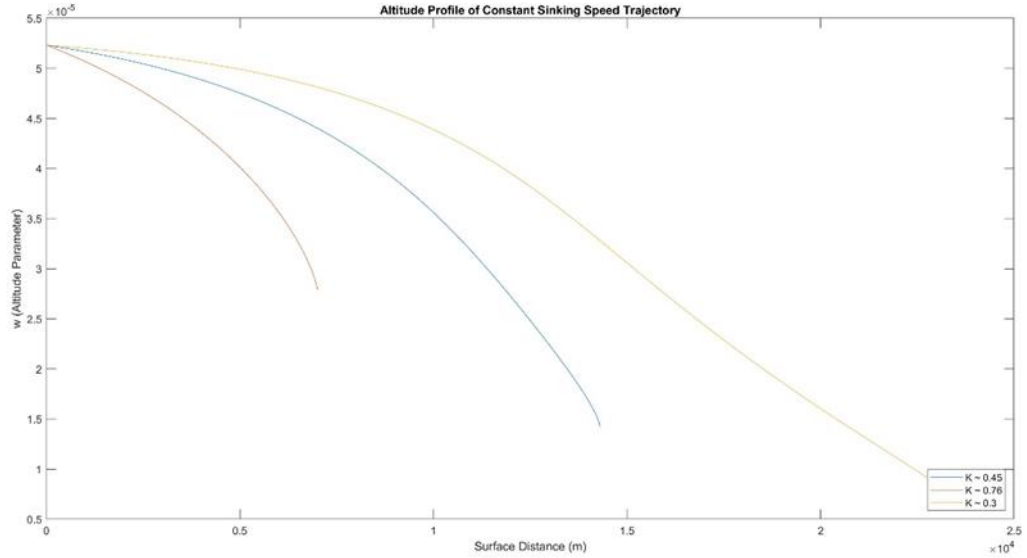

Figure 3.5: Altitude Profile of Constant Sinking Speed Trajectories

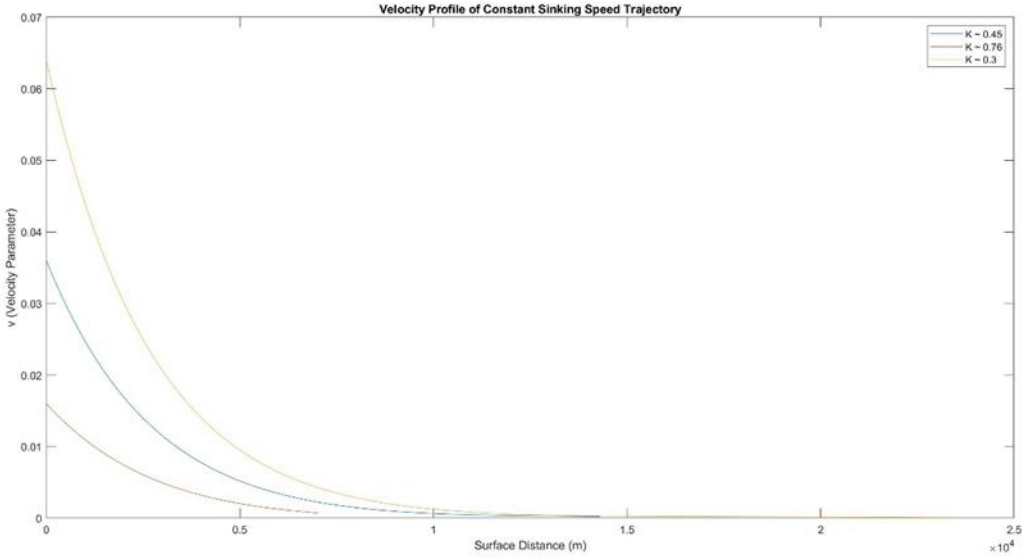

Figure 3.6: Velocity Profile of Constant Sinking Speed Trajectories

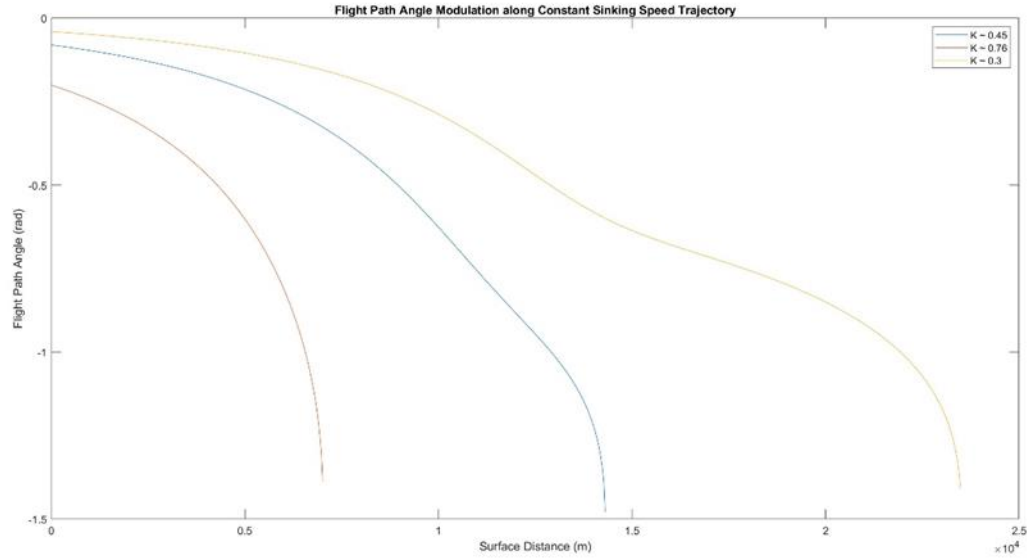

Figure 3.7: Flight Path Angle Modulation along Constant Sinking Speed Trajectories

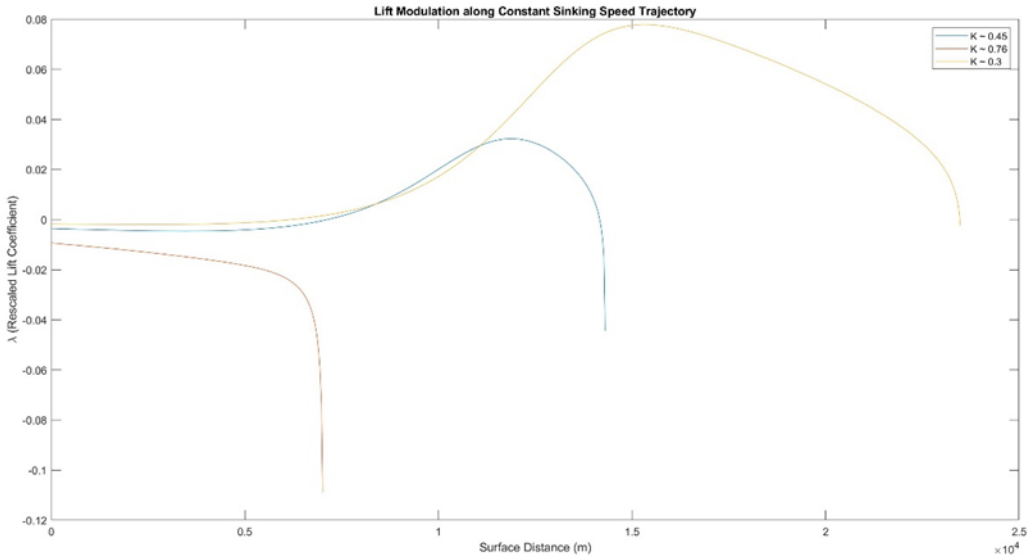

Figure 3.8: Lift Modulation along Constant Sinking Speed Trajectories

These figures show that as the chosen constant sinking speed decreases, the flight range increases. Larger constant sinking speeds drive the flight path angles higher earlier on in the trajectory, resulting in this loss of flight range and smaller overall velocities, as well as requiring negative lift generation. Therefore, the most useful of these trajectories require smaller sinking speeds for smaller flight path angles and greater velocity and range, keeping in mind that this type of trajectory is only applicable close to the surface.

3.2.3 Constant Speed

Like constant sinking speed, constant speed trajectories maintain a constant overall speed by modulating the lift and flight path angle. However, unlike the constant sinking speed trajectories, these trajectories are still useful at high altitudes. These flight profiles are depicted in Figure 3.9, Figure 3.10, and Figure 3.11 below and on the next couple pages.

Increasing the constant speed will increase the flight range but it approaches a limit set by the circular speed at the starting altitude. Figure 3.10 also shows that constant speed trajectories are achieved at very low flight path angles. This angle only sharply increases at the end of the trajectory, at which point constant speed is no longer desired. Lower constant speeds also require higher lift modulation, making high constant speeds more desirable.

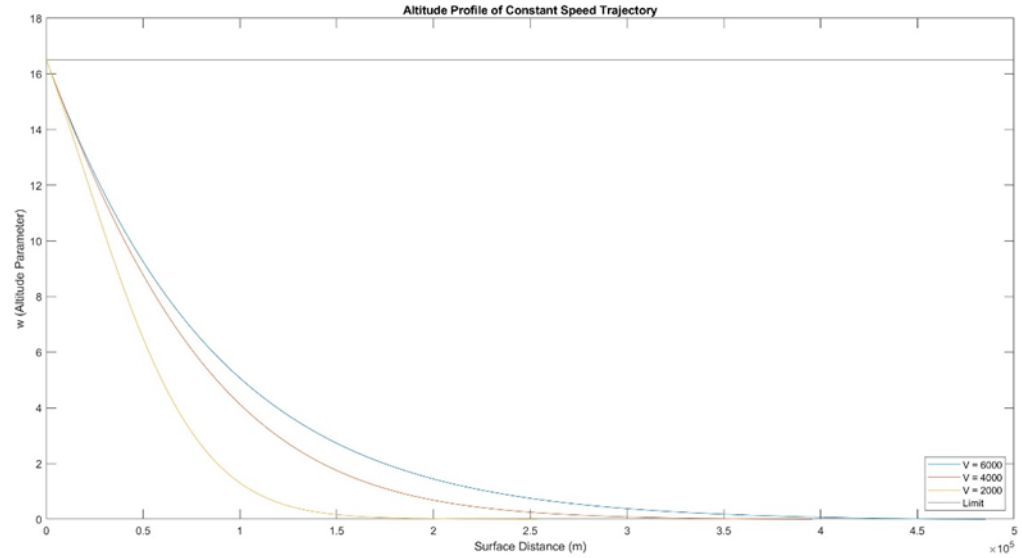

Figure 3.9: Altitude Profile of Constant Speed Trajectories

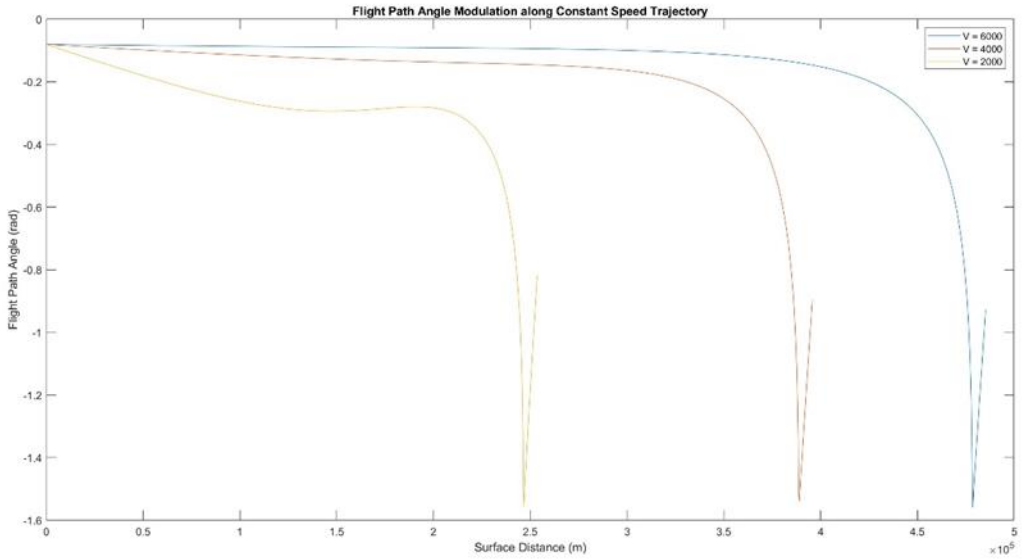

Figure 3.10: Flight Path Angle Modulation along Constant Speed Trajectories

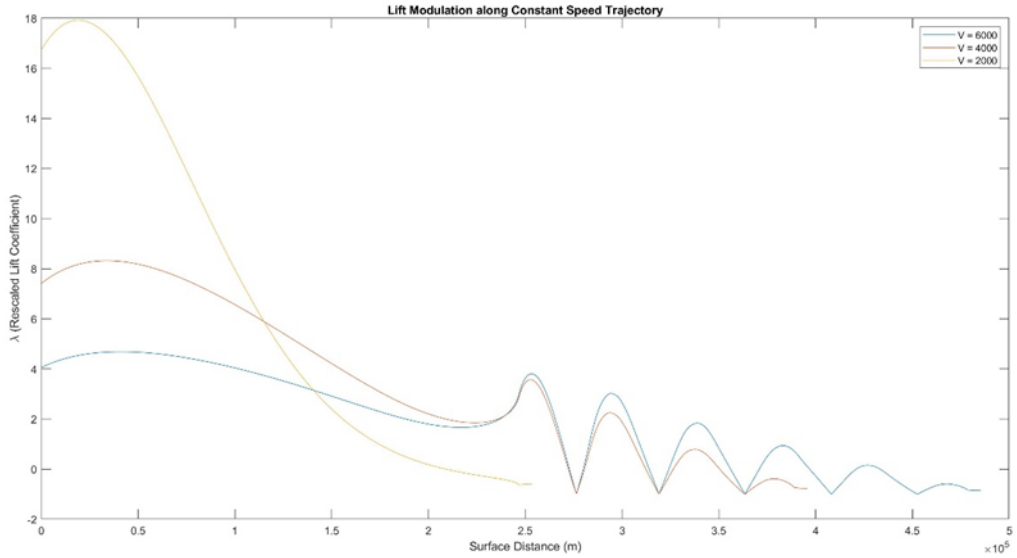

Figure 3.11: Lift Modulation along Constant Speed Trajectories

3.2.4 Constant Dynamic Pressure

Another important constraining trajectory is constant dynamic pressure. Maintaining dynamic pressure leads to optimal flight vehicle performance and fuel efficiency. This trajectory type is ideal for most of a reentry trajectory except for the final stages. Figure 3.12, Figure 3.13, Figure 3.14, and Figure 3.15 on the following pages show the profiles for some constant dynamic pressure trajectories, defined by Equation 2.48 below, where C is some constant.

$$\frac{v}{w} = C \quad (2.48)$$

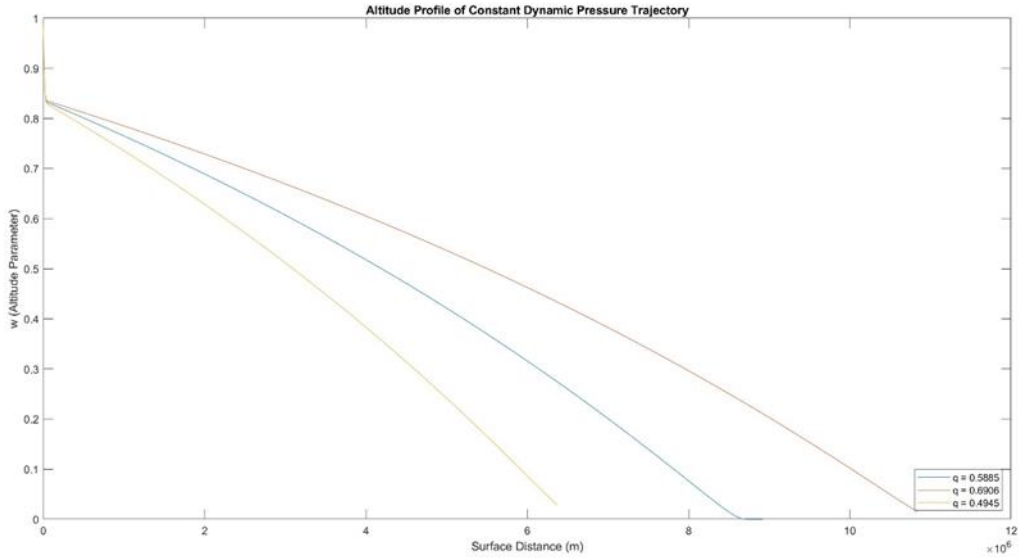

Figure 3.12: Altitude Profile of Constant Dynamic Pressure Trajectories

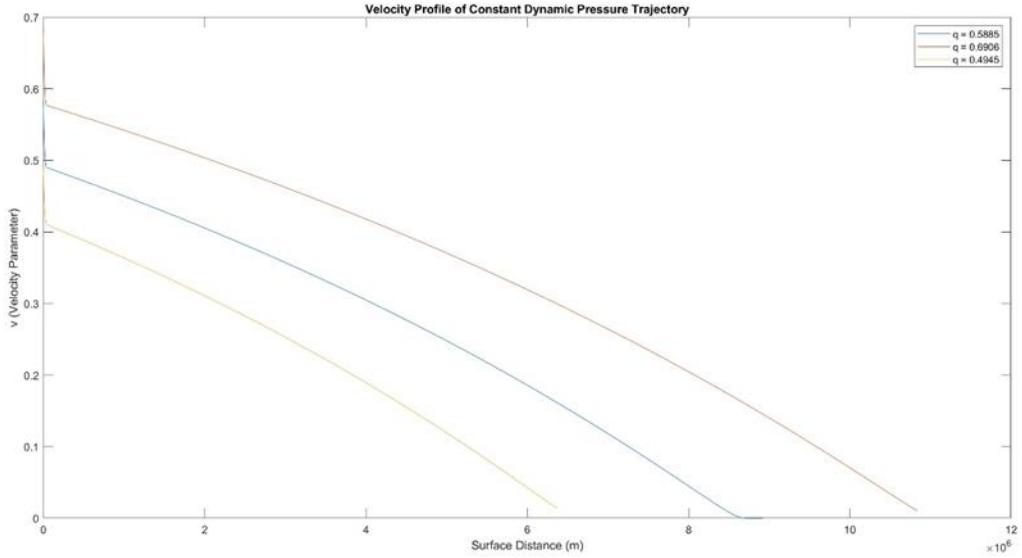

Figure 3.13: Velocity Profile of Constant Dynamic Pressure Trajectories

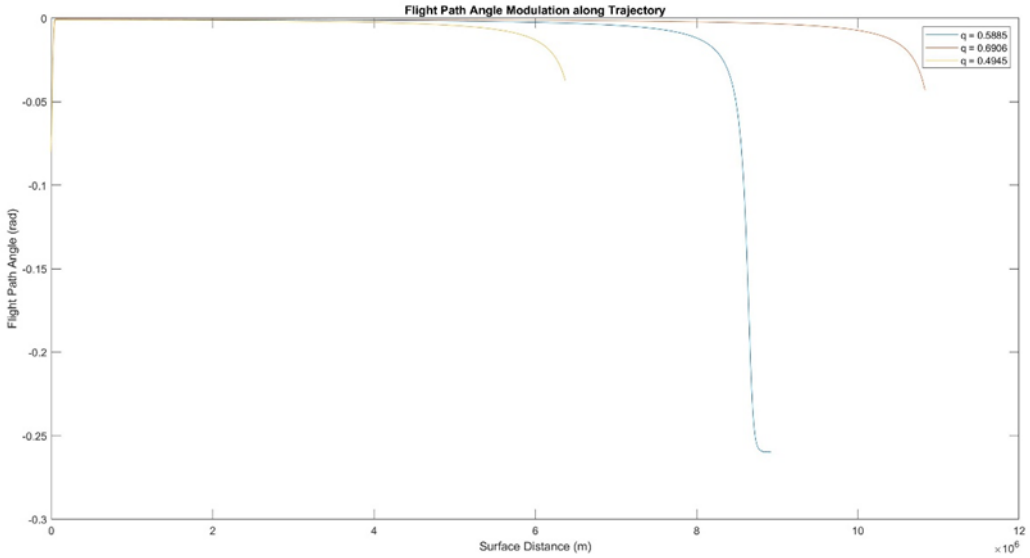

Figure 3.14: Flight Path Angle Modulation along Constant Dynamic Pressure Trajectories

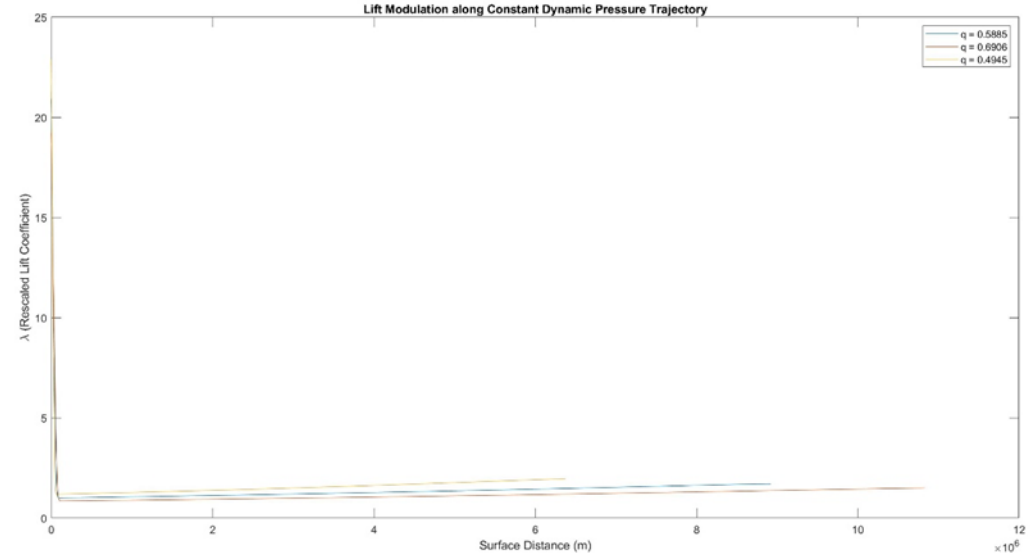

Figure 3.15: Lift Modulation along Constant Dynamic Pressure Trajectories

One of the more notable things about the constant dynamic pressure trajectory is that it occurs at negligible flight path angles with nominal lift modulation (maximum aerodynamic efficiency). For this reason, this is perhaps the most desirable type of trajectory, producing the highest flight ranges out of all five scenarios analyzed here. Increasing the constant dynamic pressure for the trajectory leads to higher flight ranges with higher velocities, but the dynamic pressure will be constrained by the structural elements of the flight vehicle.

3.2.5 Constant Heating Rate

The final glide trajectory scenario this chapter examines is the constant heating rate case. Heating rate is an important parameter because it limits what materials can be used for the flight vehicle. A constant heating rate trajectory is expressed by Equation 2.49 below and the derived trajectory profiles can be found in Figure 3.16, Figure 3.17, Figure 3.18, and Figure 3.19 on the following pages.

$$\frac{v^3}{w} = C \quad (2.49)$$

As seen in the figures, while larger allowable heating rates will provide more range and higher velocities, the lift modulation required to maintain them becomes higher than can reasonably be expected from a lift-generating flight vehicle, limiting the maximum allowable constant heating rate. Another constraint is provided by the materials used for the flight vehicle; they need to be able to withstand any maximum heating rates and maximum temperatures. While heating rate is certainly an important parameter to monitor, it may not be particularly useful to maintain a constant heating rate during reentry.

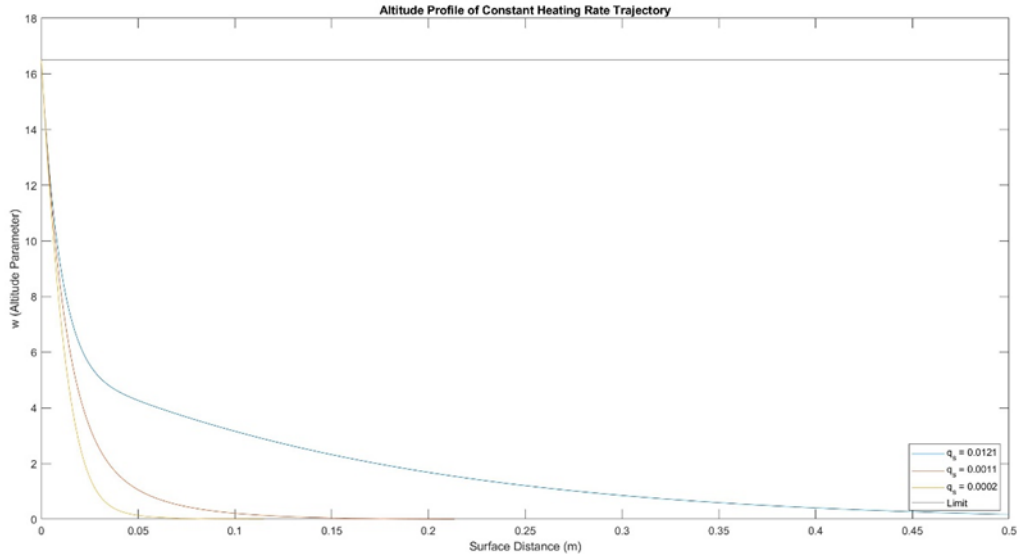

Figure 3.16: Altitude Profile of Constant Heating Rate Trajectories

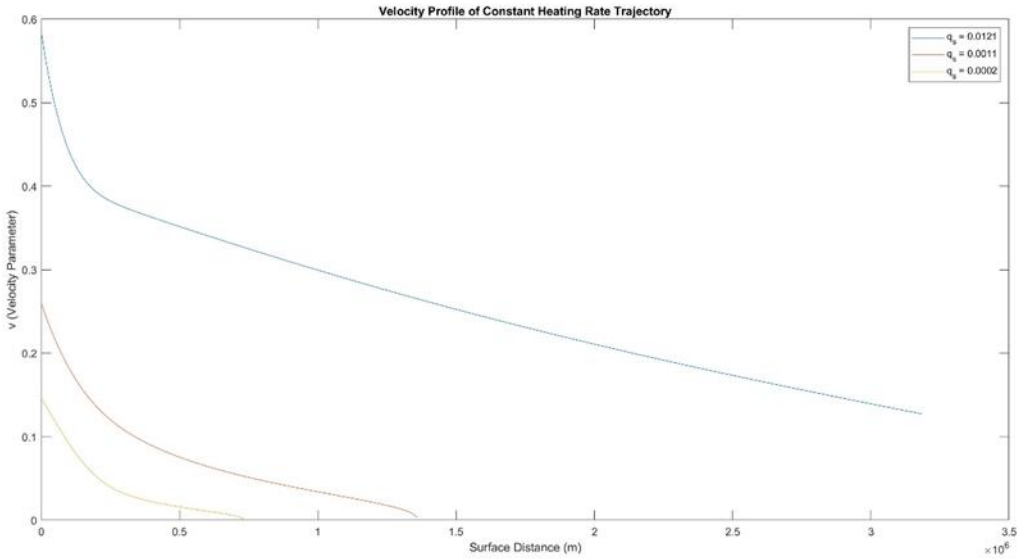

Figure 3.17: Velocity Profile of Constant Heating Rate Trajectories

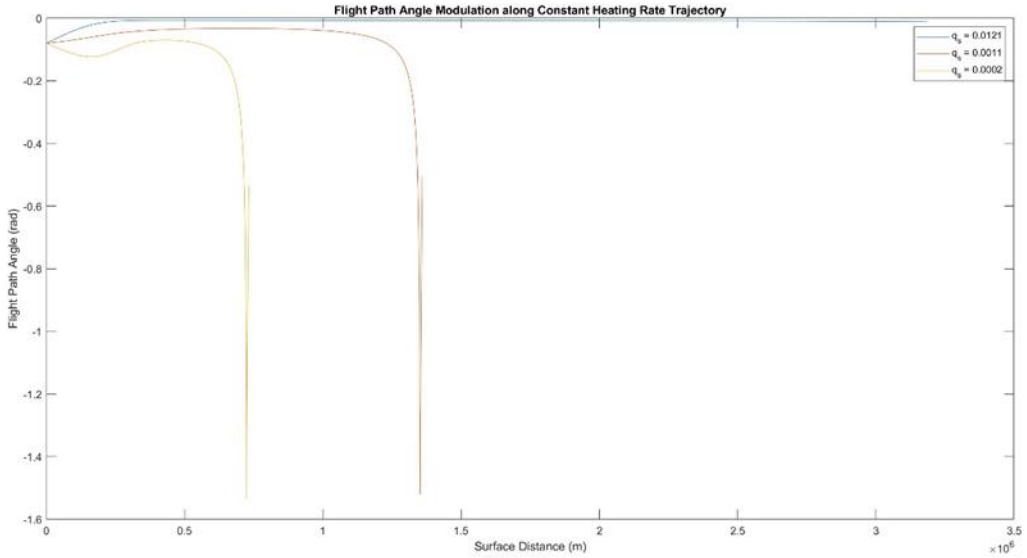

Figure 3.18: Flight Path Angle Modulation along Constant Heating Rate Trajectories

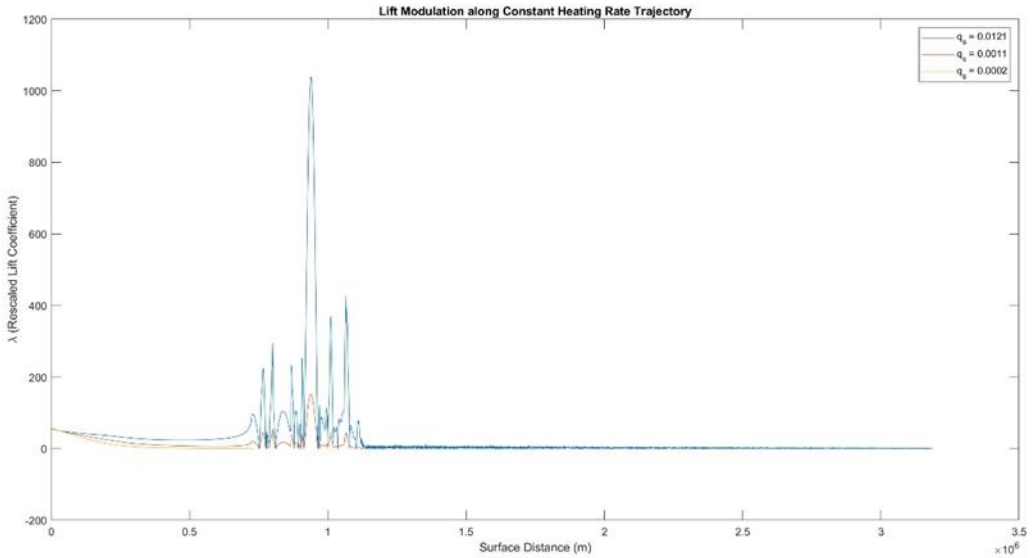

Figure 3.19: Lift Modulation along Constant Heating Rate Trajectories

3.3 Dynamic Pressure

Equation 2.48 showed how nondimensionalized dynamic pressure is calculated in general. Dynamic pressure is an important parameter since it sets the requirements for the flight vehicle's structural strength and integrity. Figure 3.20, Figure 3.21, Figure 3.22, and Figure 3.23 below and on the next two pages show example dynamic pressure profiles for the various trajectory types. From these figures, one can determine relative dynamic pressures or find the location of maximum dynamic pressure on the flight path.

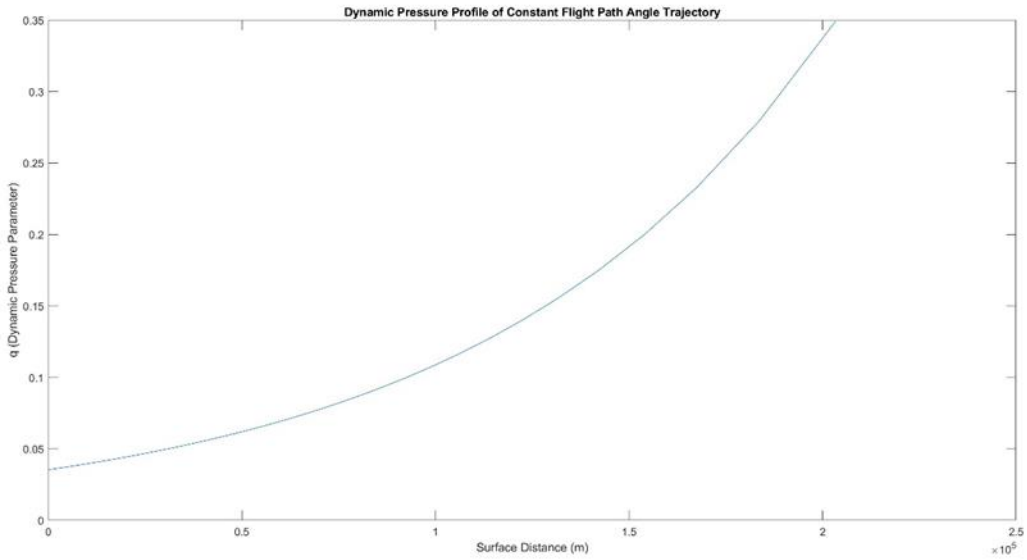

Figure 3.20: Dynamic Pressure Profile of a Constant Flight Path Angle Trajectory

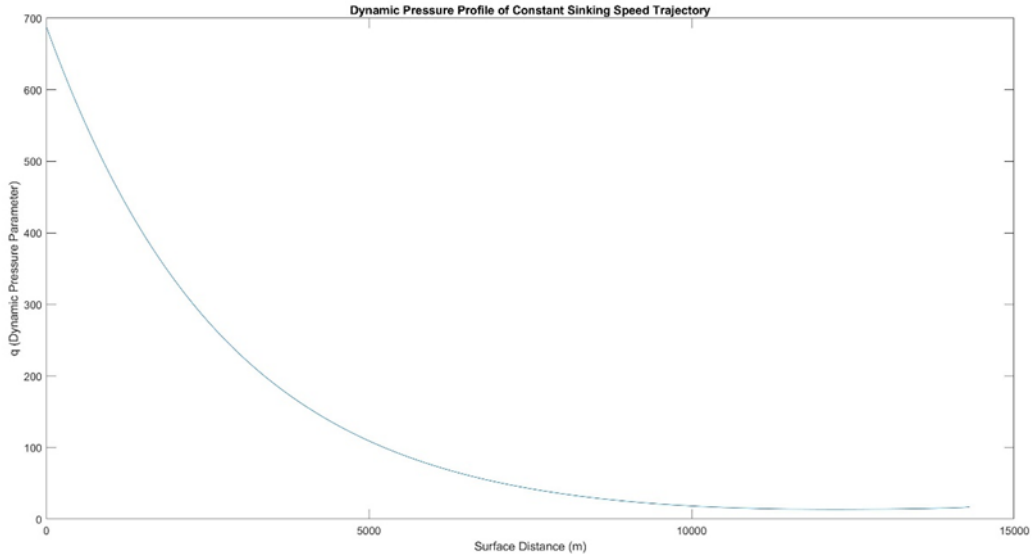

Figure 3.21: Dynamic Pressure Profile of a Constant Sinking Speed Trajectory

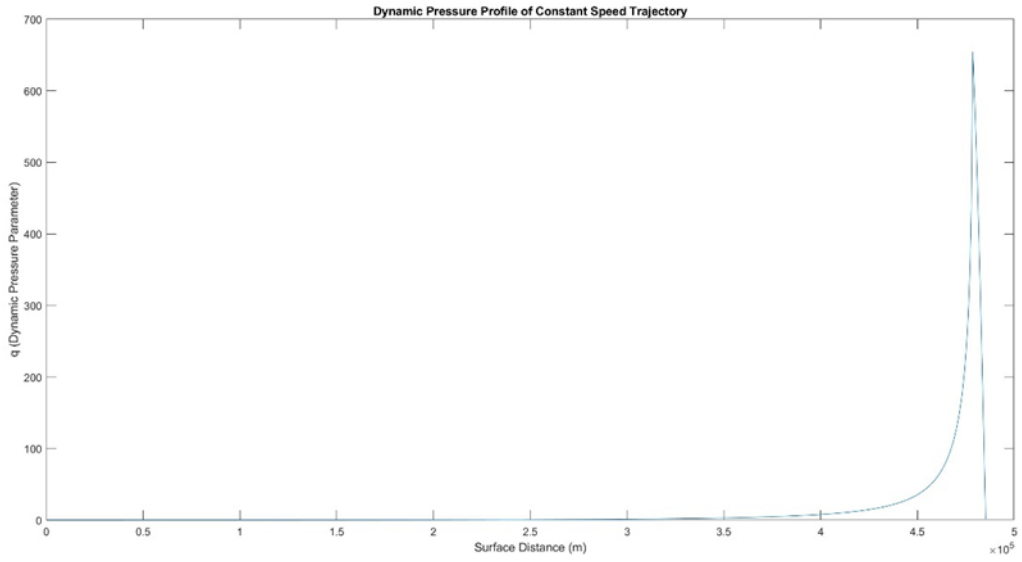

Figure 3.22: Dynamic Pressure of a Constant Speed Trajectory

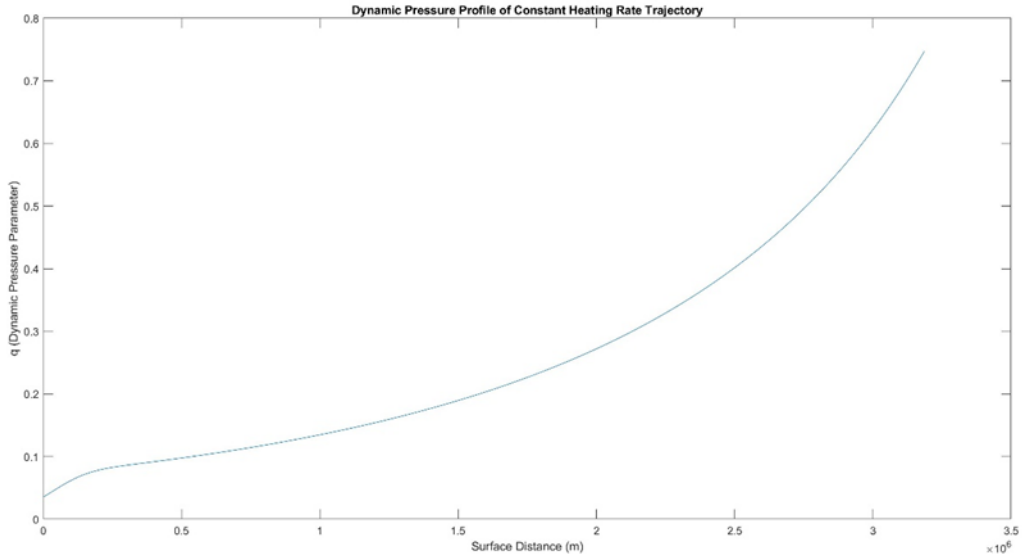

Figure 3.23: Dynamic Pressure of a Constant Heating Rate Trajectory

From these figures, almost all the trajectory types experience maximum dynamic pressure at the very end of the trajectory when the flight vehicle reaches the surface. The only exception is the constant sinking speed trajectory, which experiences its highest dynamic pressures at the beginning of the trajectory due to the high flight path angles needed to maintain the trajectory. This is one of the reasons those trajectory types are limited to low altitudes. Based on this information, when designing trajectories, the final velocity needs to be considered to limit the maximum dynamic pressure the flight vehicle experiences.

3.4 Heating Rates

Another important parameter to consider is the heating rate caused by reentry. The maximum heating rate determines the temperature requirements for the materials used for the flight vehicle. Figure 3.24, Figure 3.25, Figure 3.26, and Figure 3.27 on the following pages show the

dimensionless heating curves for the various trajectory types, allowing for comparison between the trajectories and determination of maximum heating rate. The heating rate can also be integrated over the duration of the flight path to calculate the total heating at a point on the flight vehicle.

While constant flight path angle and constant speed trajectories experience the greatest heating rate at the end, constant sinking speed and constant dynamic pressure trajectories experience it at the beginning. Since the altitude is not a controlled variable, the maximum heating rate will depend on the velocity profile of the trajectory, like dynamic pressure. However, designers will need to account for starting or final velocities depending on the trajectory type. Both the maximum heating rate and the total heating will need to be considered to prevent material failure.

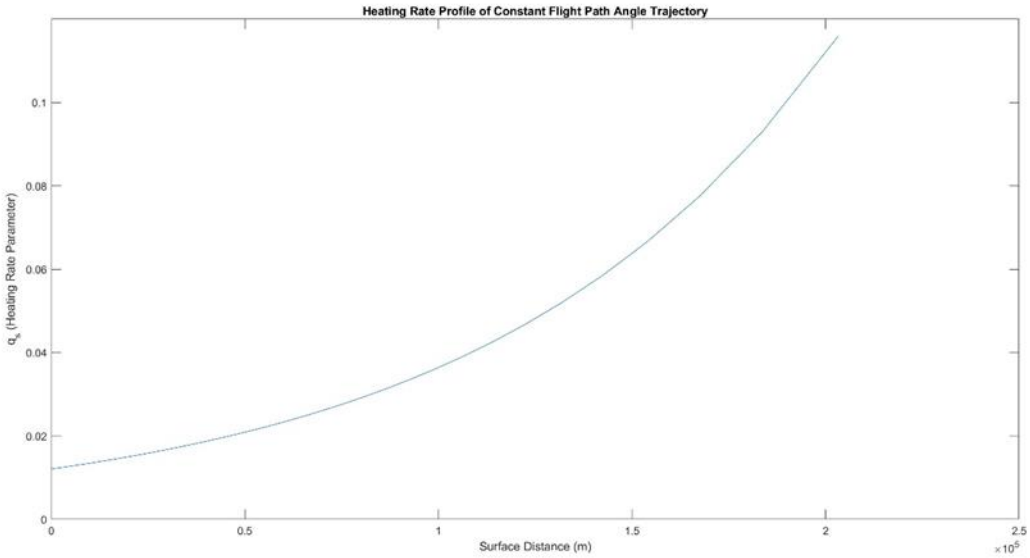

Figure 3.24: Heating Rate Profile of a Constant Flight Path Angle Trajectory

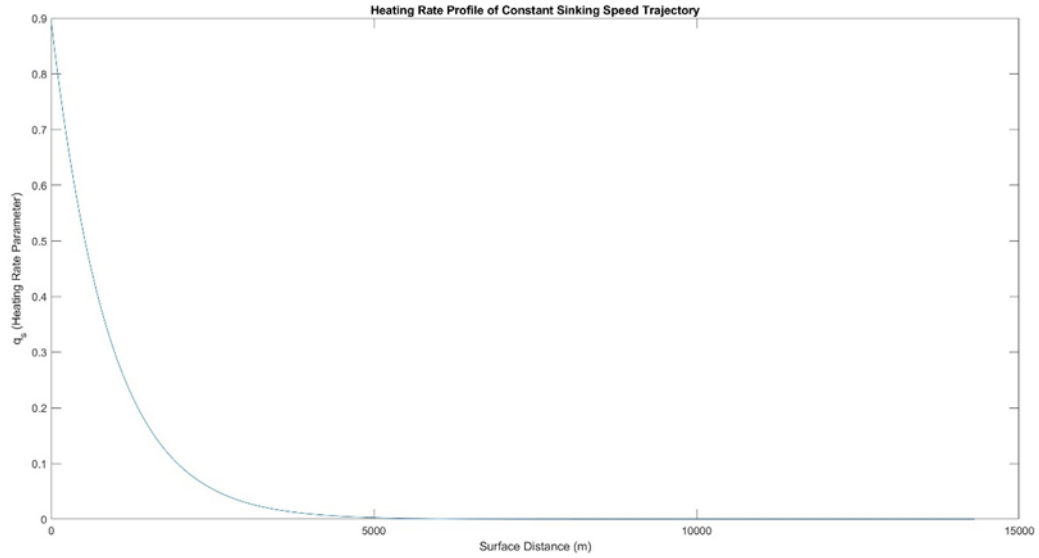

Figure 3.25: Heating Rate Profile of a Constant Sinking Speed Trajectory

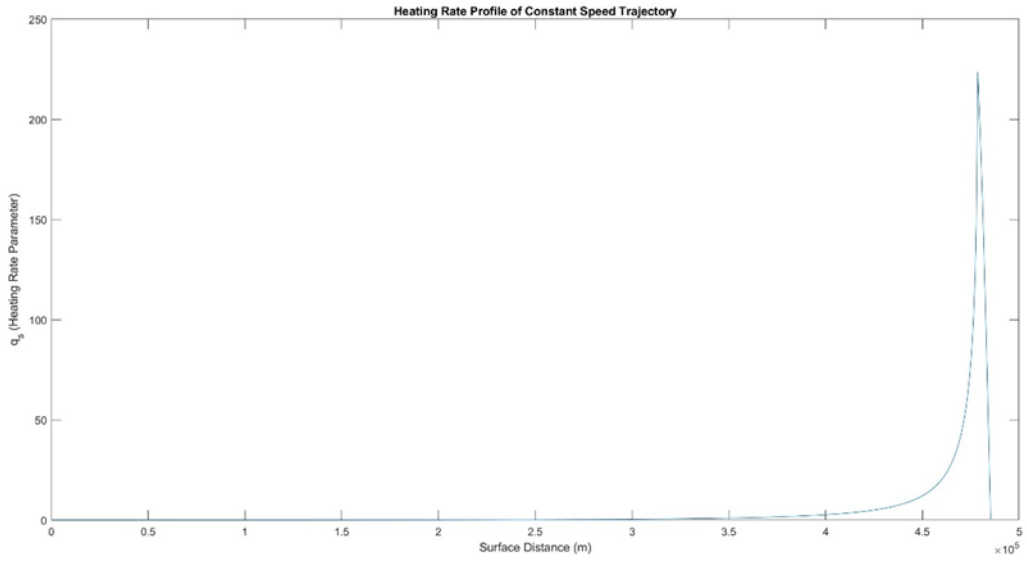

Figure 3.26: Heating Rate Profile of a Constant Speed Trajectory

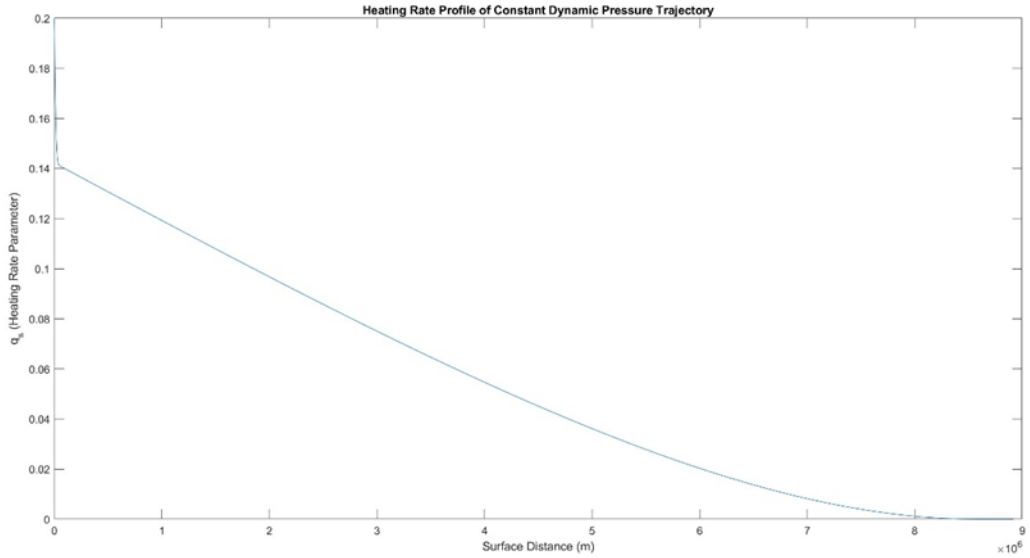

Figure 3.27: Heating Rate Profile of a Constant Dynamic Pressure Trajectory

3.5 Limitations and Requirements

By examining the altitude, velocity, flight path angle, and lift modulation profiles of a trajectory, one can determine if the trajectory is feasible or not. The trajectory designer can also impose constraints on the reentry trajectory such as maximum allowable velocity or maximum sinking speed. Additionally, the physical characteristics of the flight vehicle itself will impose limitations on maximum allowable aerodynamic heating, maximum dynamic pressure, and maximum lift generation. The designer will have to adjust the flight vehicle or trajectory design accordingly to accommodate for any existing limitations and requirements.

Chapter 4: Optimizing a Skip-Glide Reentry Trajectory

4.1 Skip Trajectory Mechanics

While glide trajectories are used for final descent through the atmosphere to the surface, skip reentry trajectories are used to dispel excess heat on a flight vehicle and extend a trajectory's range. In a skip trajectory, the flight vehicle enters the atmosphere, gliding down briefly before turning and gliding back out of the atmosphere, essentially "skipping" off the atmosphere. For the basic design and optimization purposes of this research, it was assumed that the aerodynamic efficiency of the waverider remains constant throughout this maneuver. Since the range of this maneuver is small compared to that of a glide trajectory, the "flat Earth" assumption holds. Additionally, the aerodynamic forces on the aircraft are much greater during a skip trajectory than gravity; therefore, gravity is neglected in the following analysis [19].

With a constant aerodynamic efficiency skip trajectory, the final flight path angle is equal to the absolute value of the initial flight path angle [19]. With unpowered flight, multiple skip trajectories are connected by ballistic trajectories. Because of this, the initial flight path angle for the final glide portion of the trajectory is the same as the initial flight path angle for the skip portion. Since the aerodynamic efficiency and flight path angle do not change from the beginning to the end of the skip trajectory, the only thing that is changing is the flight vehicle's velocity. As seen in Equation 4.1 below, each skip will slightly reduce the velocity available for the next skip or glide.

$$\frac{V_f}{V_i} = e^{\frac{2\gamma_i}{E}} \quad (4.1)$$

The distance covered during the skip trajectory can also be calculated from the initial flight path angle using Equations 4.2-4 shown below. Note that η is a nondimensionalized parameter corresponding to the altitude, h refers to the altitude above sea level, and γ_I represents a modified initial flight path angle used to simplify the equation.

$$\eta = \frac{SC_D\rho_0}{2m\beta} e^{-\beta h} \quad (4.2)$$

$$\cos\gamma_I = \cos\gamma_i - E\eta_i \quad (4.3)$$

$$\beta x = -2\gamma_i + \cot\gamma_I \ln\left[\left(\frac{\tan\frac{-\gamma_i}{2}+\tan\frac{\gamma_I}{2}}{\tan\frac{-\gamma_i}{2}-\tan\frac{\gamma_I}{2}}\right)\left(\frac{\tan\frac{\gamma_i}{2}-\tan\frac{\gamma_I}{2}}{\tan\frac{\gamma_i}{2}+\tan\frac{\gamma_I}{2}}\right)\right] \quad (4.4)$$

The connecting ballistic trajectories follow a parabolic arc, so their range can be calculated using Equation 4.5 below. The initial conditions here are the start of the ballistic trajectory after the completion of the skip trajectory.

$$x = \frac{V_i^2 \sin(2\gamma_i)}{g_0} \quad (4.5)$$

There are three main constraints on the skip-glide trajectory: maximum flight path angle, dynamic pressure, and aerodynamic heating. For the lowest part of the skip trajectory to still be above sea level, Equation 4.6 below must be satisfied.

$$\left(\sin\frac{\gamma_i}{2}\right)^2 < \frac{\rho_0 C_L S}{4\beta m} \quad (4.6)$$

The dynamic pressure is expressed by Equation 4.7 below. For a given flight vehicle, there will be a maximum allowable dynamic pressure, so the pressure will have to be evaluated along the trajectory.

$$P_d = \frac{\rho V^2}{2} \quad (4.7)$$

Aerodynamic heating is more difficult to analyze quantitatively. The most important parameters are the total heat input and the maximum rate of heat input per unit area. The total heat input for a skip or glide trajectory is given in Equation 2.42, provided again here.

$$Q = \frac{AC_F}{2}\left(\frac{m}{SC_D}\right) g_i r_i (u_i - u) \quad (2.42)$$

The limits for this can be estimated from the type of material used for the flight vehicle. However, evaluating the maximum rate of heat input per unit area requires detailed knowledge of the flight vehicle geometry. Due to this complication, a nondimensionalized variable is sometimes used to represent the rate of heat input, shown in Equation 4.8 below. The maximum will occur during the first skip portion of the trajectory, so realistic estimated values can be used to set a limit. Equation 4.9 below shows how to nondimensionalize the maximum heating rate limit, where q_s is the heating rate limit, R is the radius of curvature at the stagnation point, and κ is an experimentally determined constant. Additionally, this analysis is only applicable for flight velocities less than 3km/s due to the assumptions used to derive the equations [19].

$$\bar{q}_{s,max} = \frac{-u_i^{\frac{3}{2}}\gamma_i}{\sqrt{2E}} e^{\frac{3\gamma_i}{E}} \quad (4.8)$$

$$\bar{q}_s = q_s \frac{\sqrt{R}}{4\kappa}\sqrt{\frac{SC_D\rho_0}{m\beta}} \quad (4.9)$$

For the purposes of the combined skip-glide trajectory, the maximum glide range angle is calculated using Equation 4.10 and 4.11 below [2].

$$\theta = \frac{E}{2}\ln\left(\frac{1}{1-{V_r}^2}\right) \quad (4.10)$$

$$V_r = \frac{V_i}{\sqrt{\frac{\mu}{r_i}}} \quad (4.11)$$

4.2 Optimization Scenario

For an initial attempt at skip-glide trajectory optimization, a basic scenario is used to provide better insight into the analysis. In this scenario, a hypersonic waverider is entering the Earth's atmosphere, traveling along the equator in a skip-glide trajectory. The goal is to maximize the total range of the trajectory, while staying within the flight path angle, dynamic pressure, and aerodynamic heating limitations. Given the flight vehicle characteristics, planetary body characteristics, initial velocity, and initial altitude, the initial flight path angle, aerodynamic efficiency, and number of skips will be traded to determine the optimal trajectory to maximize range.

The following flight vehicle characteristics were used for this analysis: a wing surface area of 360m^2, a nose radius of 0.71m, a mass of 6,000kg, and a drag coefficient of 0.003125. The specific characteristics used in this scenario are not very important to the procedure of optimizing trajectories but were used to calculate values for the nondimensionalized variables in the analysis. The planetary body characteristics used were values provided for the Earth by Vinh, et al [19]. The average scale height was 7.1km, the sea level air density was 1.225kg/m^3, the sea level radial distance was 6,371.146km, the average nondimensionalized scale height factor was 900, and the gravitational parameter was 398,600km^3/s^2. For this scenario, an initial altitude of 100km was used, since this is about the starting altitude of the Earth's atmosphere, as well as initial velocities of 2, 2.5, 3, and 3.5km/s. At the highest velocity, the assumptions made earlier no longer necessarily apply, but the results still give valuable insight into potential optimal trajectories.

To streamline the optimization process, instead of analyzing an open-ended range of values, the following ranges for the driving parameters were determined beforehand. The number

of skips varied between zero and five; if the maximum range occurred with five skips, it could be extrapolated that more skips would add more range (to an extent). For the aerodynamic efficiency, values between 3 and 15 were used to generate the design space; however, constraints were set limiting valid trajectories between efficiencies of 6 and 12 based on the lift-to-drag ratios used in Nguyen's case studies. High efficiencies are necessary for the waverider to maintain stability, but there are limits on the maximum efficiency physically achievable. Additionally, the flight path angles chosen were also based off Nguyen's work, ranging from 0.1 to 45 degrees [2].

The dynamic pressure limitation was borrowed from a hypersonic flight vehicle analysis performed by Chamitoff, namely 95kPa [23]. Another study, by Rizvi, et al., informed the maximum heating value used in this scenario, $4MW/m^2$ [12]. Normally an experimentally-determined stagnation temperature heating rate constant is used to determine the nondimensionalized heating rate limit. For demonstrating this analysis methodology, based on the nondimensionalized heating rate values calculated for the various trajectories, it was determined that a constant of $96{,}500W/m^{3/2}$ would be used to make the maximum limit have the same order of magnitude. These maximum dynamic pressure and heating rate values were used to constrain the reentry trajectory in this scenario.

4.3 Optimization Strategy

This research employed a classical optimization approach, using graphical representations in MATLAB of the data and design space to determine an optimized solution [17]. To show the workable design space, carpet plots were used to plot two independent variables, in this case the initial flight path angle and aerodynamic efficiency, versus a dependent variable, the range angle.

The higher a point is on the y-axis, the higher the range, which is the goal of the optimization [16]. One carpet plot was used to represent each skip number at each initial velocity.

Once the design space was created, the constraining curves were mapped onto the carpet plot to show how they constrained the solutions. From this procedure, it was determined that the maximum flight path angle constraint for all cases was well above the maximum angle of 45 degrees analyzed in this research. As a result, it was not portrayed on the carpet plots. On the other hand, the maximum heating rate was found to actively affect some of the trajectory solutions. When applicable, this constraint divided the design space into three sections; valid trajectories existed above one constraint curve while more valid trajectories existed below another one. Since the section above the first heating constraint curve provided higher range angles than the other section, therefore more actively constraining the solutions, the carpet plots affected only show the first heating constraint curve. The main constraint active in this optimization was the dynamic pressure, providing an upper bound on the achievable range angle.

Therefore, in the design spaces represented by the carpet plots, valid solutions mainly exist between the upper bounding maximum dynamic pressure curve and the lower bounding maximum heating rate curve. Within this section, it is possible to determine the maximum range angle and the corresponding initial flight path angle and aerodynamic efficiency. These can then be compared across all analyzed skip numbers for a given initial velocity to find the overall optimized trajectory for that initial flight speed and given initial conditions.

4.4 Optimization Results

After analyzing the scenario outlined above, carpet plots were made for the four initial fight speeds. Based on a numerical and graphical examination of the range data, at each initial flight speed, the overall maximum range occurred during the five-skip case. In Figure 4.1 below, the carpet plot shows the design space for the five-skip case at 3km/s. The maximum heating rate constraint is shown in red, the maximum dynamic pressure constraint is shown in blue, and the aerodynamic efficiency constraints are shown in green. Allowable trajectories lie between the four constraint curves on the carpet plot. The maximum allowable range angle case is marked with a black 'x' in the figure.

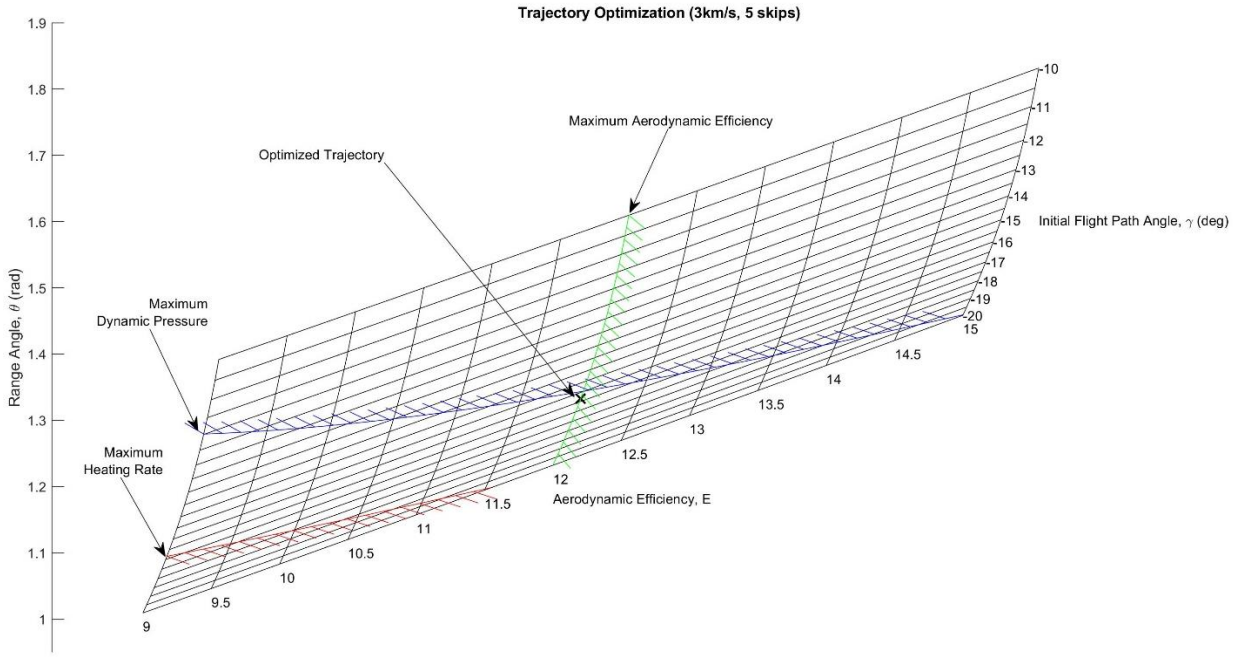

Figure 4.1: Carpet Plot Showing the Optimized Trajectory for the 5-Skip Case at 3km/s

The maximum allowable range angle for the provided scenario was 1.3324 radians (equivalent to about 76 degrees). This value corresponds to a range of approximately 8,500 km, about 21% of the Earth's circumference. As mentioned previously, since the maximum heating rate occurs during the first skip and the maximum dynamic pressure decreases with the number of skips, the maximum range could be extended further using more skips. However, since some speed is lost during each skip into the atmosphere, there is a point where it becomes more advantageous to glide the rest of the way instead of continuing to skip.

For this maximum range trajectory, the corresponding flight path angle was -16.35 degrees, and the corresponding aerodynamic efficiency was 12, the maximum efficiency analyzed. According to the carpet plot above, for a given aerodynamic efficiency, the range angle increases as the magnitude of the flight path angle decreases. At this flight speed, the range angle increases with increasing aerodynamic efficiency. At other initial velocities or other initial conditions, it will be shown that sometimes the opposite is true, where increasing aerodynamic efficiency decreases the range angle, resulting in a lower optimal aerodynamic efficiency.

If the imposed maximum allowable dynamic pressure was increased, represented by the blue curve translating higher on the carpet plot, then the maximum range angle would also increase. The absolute value of the flight path angle for this trajectory would decrease; however, the aerodynamic efficiency would remain the same. On the other hand, relaxing the maximum heating rate constraint would not affect the maximum allowable range angle, although it would provide more permissible solutions. Decreasing the heating rate limit would translate the red curve lower on the carpet plot. Similarly, increasing the heating rate limit would translate it higher. If the heating rate limit were significantly increased, it could theoretically overtake the dynamic

pressure constraint, leaving no feasible trajectory solutions. Since an arbitrary heat-transfer constant was chosen for this analysis, it could be the case that physical experiments provide a different heating rate limit than the one used in this paper. One final thing to note about this particular initial flight speed is that it is right at the limit for the assumptions made in the analysis. Around this point, experimental results will begin to deviate from the trends outlined in the analysis equations.

Figure 4.2 on the next page shows the design space for an initial flight speed of 3.5km/s. Since this speed is above the limitations set for the assumptions, its solutions are not necessarily valid, but will give a general idea of possible solutions and where they might lie. Therefore, an analysis of this flight speed is still useful for design purposes. However, the assumed heating rate constraint used previously turned out to be too high for this set of conditions; the maximum heating rate curve was above the maximum dynamic pressure curve. For this flight speed only, the stagnation temperature heating rate constant was lowered to 55,000W/$m^{3/2}$ just to observe where the optimized trajectory would be constrained only by the dynamic pressure and aerodynamic efficiency. As seen in the plot, the maximum range is 1.3766 radians at an initial flight path angle of -26.92 degrees and aerodynamic efficiency of 12. Ignoring the heating constraint issue, increasing the flight speed will increase the range angle while requiring a steeper flight path angle.

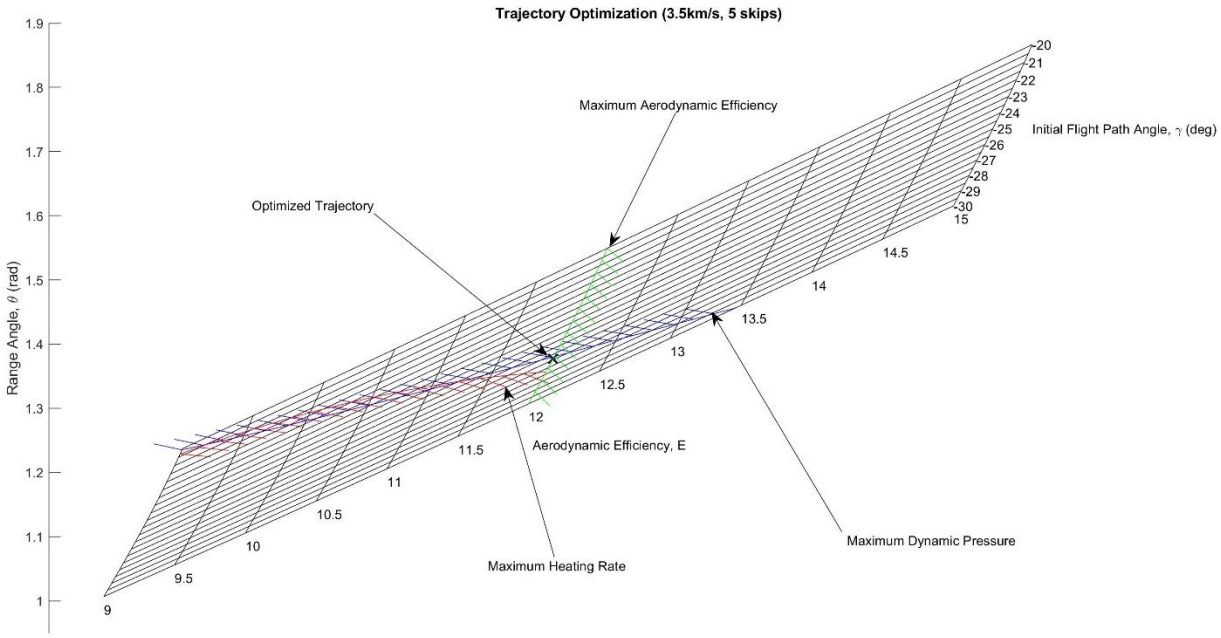

Figure 4.2: Carpet Plot Showing the Optimized Trajectory for the 5-Skip Case at 3.5km/s

Figure 4.3 and Figure 4.4 on the following pages show the design spaces for the cases of 2 and 2.5km/s initial flight speeds, respectively. In both carpet plots, the maximum heating rate curve is no longer visible, showing it is not an active constraint for these cases. Additionally, the 2km/s case does not have an active maximum dynamic pressure constraint, limited only by the minimum aerodynamic heating value. For this case, the range is 16.5578 radians at a -0.1 degree flight path angle and aerodynamic efficiency of 6. At 2.5km/s, the range is 3.1897 with an initial flight path angle of -1.9 at the same aerodynamic efficiency. All these values, as well as the ones provided above, are summarized in Table 4.1 following the figures. The main take away from these two cases is that by lowering the initial flight speed and flight path angle, the maximum range of the trajectory can be extended, potentially by several factors. However, it may or may not be feasible to use initial flight path angles that small in magnitude. Also, it is important to note that the

maximum range angle occurs at the minimum aerodynamic efficiency value. As mentioned previously, at these lower flight path angles, the range angle actually decreases as aerodynamic efficiency increases. Since it may be important for the flight vehicle to have a higher aerodynamic efficiency for other portions of its mission, it is useful to note that at 2.5km/s, increasing the aerodynamic efficiency does not significantly decrease the maximum range angle like it does at 2km/s.

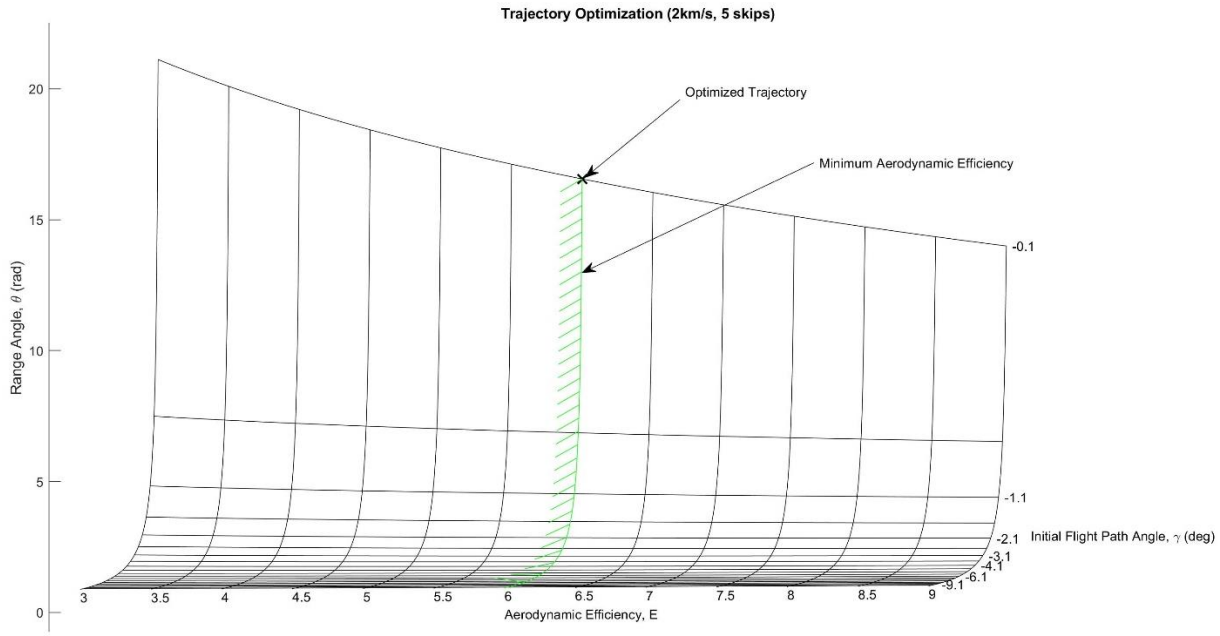

Figure 4.3: Carpet Plot Showing the Optimized Trajectory for the 5-Skip Case at 2km/s

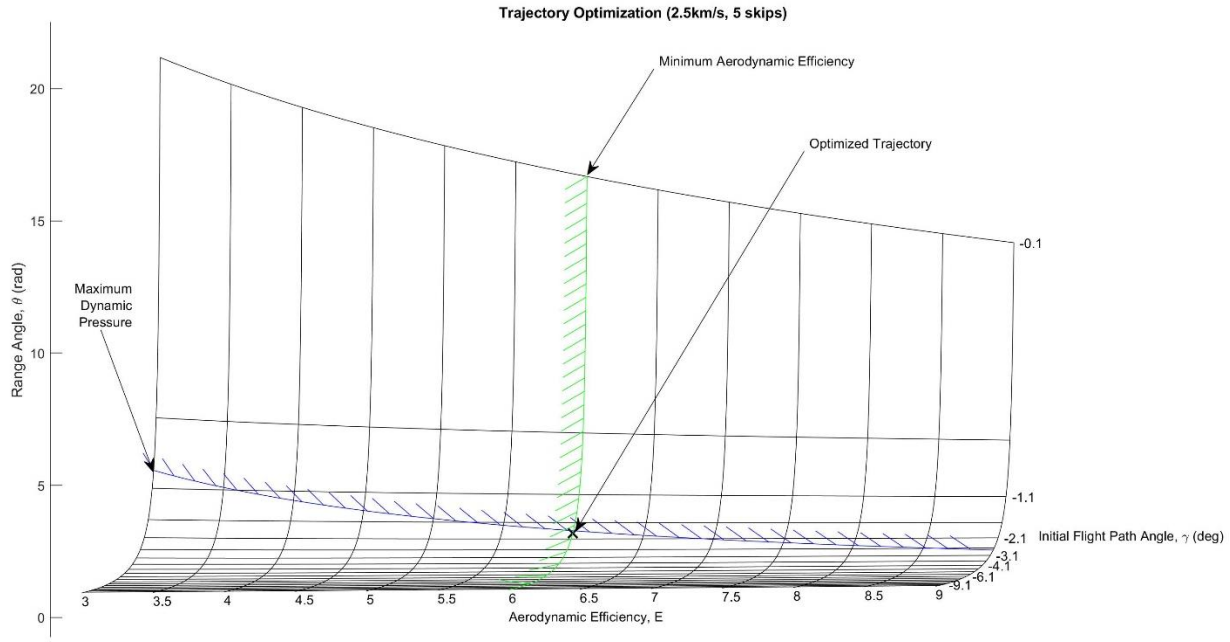

Figure 4.4: Carpet Plot Showing the Optimized Trajectory for the 5-Skip Case at 2.5km/s

Table 4.1: Summary of Trajectory Optimization Results

Initial Flight Speed (m/s)	Heating Rate Constant (W/m^(1.5))	Number of Skips	Initial Flight Path Angle (deg)	Aerodynamic Efficiency	Range angle (rad)
2000	96500	5	-0.1	6	16.5578
2500	96500	5	-1.898	6	3.1897
3000	96500	5	-16.35	12	1.3324
3500	55000	5	-26.92	12	1.3766

4.5 Uncertainty and Error Analysis

Since this research presents a preliminary analysis and optimization used to inform basic hypersonic waverider design, several assumptions were used that would introduce error in the results. The assumptions required for the unified theory for reentry flight mechanics will introduce a small amount of error. As mentioned before, analyzing initial flight speeds above 3km/s will introduce a large amount of error since it violates the assumptions used in the analysis.

This analysis also applied hypersonic reentry flight mechanics to the entire reentry trajectory. However, since the flight speed decreases later in the trajectory, these flight mechanics will no longer be applicable near the end of the trajectory. This will introduce error in the achievable range angles for the trajectory but should not affect the initial flight path angle and aerodynamic efficiency optimization results. Finally, these trajectories also assume flight through an ideal gas with no shock/boundary layer interactions. Adding in these real effects could change the results of the analysis but not significantly.

4.6 Powered Entry Trajectories

While this research and analysis has focused primarily on unpowered atmospheric reentry, the trajectory ranges found here could be extended even further by utilizing onboard propulsion systems. The additional velocity provided by the propulsion could be used to cruise in the atmosphere before gliding or to provide more velocity during the skips, as explored in Nguyen's research [2]. Unfortunately, no completely operational air-breathing hypersonic propulsion system exists today, at least as known by the public. The only way to achieve this additional velocity would be via small rocket engines attached to the waverider. However, several systems are currently being researched and designed, such as scramjets that could be incorporated into the body of the waverider [22,23,24]. It is therefore important to take the scramjet or comparable propulsion system into account when designing these hypersonic waveriders.

Chapter 5: Conclusion and Further Work

5.1 Conclusions

The goal of this research was to analyze the flight mechanics for hypersonic atmospheric reentry and use this analysis to optimize skip-glide trajectories for Earth equatorial reentry. To do so, a classical optimization methodology for determining an optimal hypersonic trajectory that fit within provided constraints was introduced and demonstrated for the given scenario. The carpet plots provided showed the results of the graphical optimization for four different initial flight speeds. At the nominal flight speed of 3km/s and an initial altitude of 100km, the resulting optimal trajectory covered 21% of the Earth's circumference with an initial flight path angle of -16.35 degrees and constant aerodynamic efficiency of 12. The active constraints in this analysis were determined to be the maximum dynamic pressure and limitations on aerodynamic efficiency. Reducing the flight speed to 2.5 or even 2km/s increased the maximum range angle achievable while lowering the required initial flight path angles and aerodynamic efficiencies.

These results can be used to inform future hypersonic waverider design, which is dependent on aerodynamic efficiency and nominal flight speed. Additionally, the optimization process can be used in mission design to extend flight ranges, increasing mission capabilities. This methodology is also not limited to the Earth and its atmosphere. Since the analysis uses nondimensionalized variables, as long as the initial conditions, flight vehicle characteristics, and planetary body characteristics are known, it can be used for atmospheric entry on other planets.

5.2 Future Work

In the future, this research could be expanded by increasing the number of skips in the trajectories or by exploring different ranges for the initial flight path angle and aerodynamic efficiency. Additionally, experimental data would better inform the dynamic pressure and heating rate constraints used in this research. The methods used here could be demonstrated for other Earth atmosphere scenarios or for entry into other planet's atmospheres. Moreover, other optimization techniques could be applied to this same scenario, such as a numerical optimization or an online trajectory generation. The flight mechanics used in this scenario were based on several underlying assumptions (nonrotating Earth, exponential atmosphere, etc.), so future work could also analyze more generic cases not limited to those assumptions or find new assumptions for analyzing higher initial flight speeds. The optimization results reported here could be used to form a basic design for an optimal hypersonic waverider for the scenario. Finally, future research could optimize trajectories for hypersonic waveriders with scramjet propulsion systems and explore the implications of powered reentry.

References

[1] Bertin, J. J., and Cummings, R. M., "Fifty years of hypersonics: where we've been, where we're going," *Progress in Aerospace Sciences* [online journal], Vol. 39, 2003, pp. 511-536.
doi: 10.1016/S0376-0421(03)00079-4

[2] Nguyen, N.-T. D., "Performance Analysis of Skip-Glide Trajectories for Hypersonic Waveriders in Planetary Exploration," Master's Thesis, Univ. of Tennessee, Knoxville, TN, 2008.

[3] Gaitonde, D. V., "Introduction to Hypersonic Flow," *Encyclopedia of Aerospace Engineering* [online journal], 2010.
doi: 10.1002/9780470686652.eae035

[4] Hirschel, E. H., *Basics of Aerothermodynamics*, Springer, New York, NY, 2005.

[5] Anderson, J. D., Jr., Lewis, M. J., and Kothari, A. P., "Hypersonic Waveriders for Planetary Atmospheres," *Journal of Spacecraft and Rockets* [online journal], Vol. 28, No. 4, 1991, pp. 401-410.
doi: 10.2514/3.26259

[6] Scott, J., "Hypersonic Waveriders," *Aerospace Web* [online database], 2000, URL: http://www.aerospaceweb.org/design/waverider/main.shtml [retrieved 7 March 2021].

[7] Tincher, D. T., and Burnett, D. W., "Hypersonic Waverider Test Vehicle: A Logical Next Step," Journal of Spacecraft and Rockets [online journal], Vol. 31, No. 3, 1994, pp. 392-399.
doi: 10.2514/3.26451

[8] Eggers, A. J., Jr., Allen, H. J., and Neice, S. E., "A Comparative Analysis of the Performance of Long-Range Hypervelocity Vehicles," NACA Report 1382, 1958.

[9] Rudd, L. V., Pines, D. J., and Carter, P. H., II, "Improved Performance of Sub-Optimal Periodic Hypersonic Cruise Trajectories for Long Range," AIAA Paper 98-1585, 1998.

[10] Carter, P. H., II, Pines, D. J., and Rudd, L. V., "Approximate Performance of Periodic Hypersonic Cruise Trajectories for Global Reach," *Journal of Aircraft* [online journal], Vol. 35, No. 6, 1998, pp. 857-867.
doi: 10.2514/2.2405

[11] Palumbo, R., Morani, G., and Cicala, M., "Reentry Trajectory Optimization for Mission Analysis," *Journal of Spacecraft and Rockets* [online journal], Vol. 54, No. 1, 2017.
doi: 10.2514/1.A33465

[12] Rizvi, S. T. U. I., Shah, S. I. A., Linshu, H., and Dajun, X., "Trajectory Optimization for a Rocket-Assisted Hypersonic Boost-glide vehicle," *Aeronautical Journal* [online journal], (Mar.) 2017.
doi: 10.1017/aer.2017.11

[13] Maxwell, J. R., and Phoenix, A., "Morphable Hypersonic Waverider and Trajectory Optimized for Atmospheric Entry," AIAA Paper 2017-5357, 2017.
doi: 10.2514/6.2017-5357

[14] Zhao, J., Zhou, R., and Jin, X., "Progress in reentry trajectory planning for hypersonic vehicle," *Journal of Systems Engineering and Electronics* [online journal], Vol. 25, No. 4, pp. 627-639.
doi: 10.1109/JSEE.2014.00073

[15] Tillier, C. "Skip reentry trajectory.svg," *Wikimedia* [online database], 2014, URL: https://commons.wikimedia.org/wiki/File:Skip_reentry_trajectory.svg [retrieved 7 March 2021].

[16] Raymer, D. P., *Aircraft Design: A Conceptual Approach*, AIAA Education Series, AIAA, New York, 1992, Chap. 19.

[17] Aultman, M., "Investigation into Geometric Parameters of an Inverted Airfoil in Ground Effect with the Utilization of Classic Optimization Techniques," Undergraduate Research Thesis, Dept. of Mechanical and Aerospace Engineering, Ohio State Univ., Columbus, OH, 2017.

[18] Miele, A., *Flight Mechanics, Vol.1: Theory of Flight Paths*, Addison-Wesley, Reading, MA, 1962.

[19] Vinh, N. X., Busemann, A., and Culp, R. D., *Hypersonic and Planetary Entry Flight Mechanics*, Univ. of Michigan, Ann Arbor, MI, 1980.

[20] Chapman, D. R., "An Approximate Analytical Method for Studying Entry into Planetary Atmospheres," NACA Technical Note 4276, 1958.

[21] Brace, F. C., "An Improved Chapman Theory for Studying Entry into Planetary Atmospheres," Ph. D. Thesis, Univ. of Michigan, Ann Arbor, MI, 1974.

[22] Allen, H. J., and Eggers, A. J., Jr., "A Study of the Motion and Aerodynamic Heating of Missiles Entering the Earth's Atmosphere at High Supersonic Speeds," NACA Technical Report 1381, 1958.

[23] Chamitoff, G. E., "An Intelligent Approach to Robust Real-Time Trajectory Control for Advanced Flight Vehicles," *International Federation of Automatic Control Proceedings* [online journal], Vol. 26, No. 1, 1993, pp. 306-311.
doi: 10.1016/S1474-6670(17)49317-7

[24] Choubey, G., Yuvarajan, D., Huang, W., Shafee, A., and Pandey, K. M., "Recent Research Progress on Transverse Injection Technique for Scramjet Applications-A Brief Review," *International Journal of Hydrogen Energy* [online journal], Vol. 45, 2020, pp. 27806-27827.
doi: 10.1016/j.ijhydene.2020.07.098

[25] Zhao, Z., Huang, W., Yan, L., and Yang, Y., "An Overview of Research on Wide-Speed Range Waverider Configuration," *Progress in Aerospace Sciences* [online journal], Vol. 113, 2020, pp. 1-14.
doi: 10.1016/j.paerosci.2020.100606

[26] Youyin, W., Kunlin, C., Jingfeng, T., Xiaoyong, L., and Wen, B., "Analysis of the Maximum Flight Mach Number of Hydrocarbon-Fueled Scramjet Engines under the Flight Cruising Constraint and the Combustor Cooling Requirement," *Aerospace Science and Technology* [online journal], Vol. 98, 2020, pp. 1-12.
doi: 10.1016/j.ast.2019.105594